Available online at www.sciencedirect.com
ScienceDirect
Lithos 92 (2006) 588–608
LITHOS
www.elsevier.com/locate/lithos

Petrology and mineralogy of granulite-facies mafic xenoliths (Sardinia, Italy): Evidence for KCl metasomatism in the lower crust

Alessandra Montanini [a,*], Daniel Harlov [b]

[a] *Dipartimento di Scienze della Terra, Università di Parma, Parco Area delle Scienze 157 a, 43100 Parma, Italy*
[b] *GeoForschungsZentrum Potsdam, Telegrafenberg, D-14473 Potsdam, FR Germany*

Received 8 July 2005; accepted 30 March 2006
Available online 30 June 2006

Abstract

Here new mineralogical data is presented on the occurrence of K-feldspar in granulite-facies metagabbronorite xenoliths found in recent alkaline lavas from Western Sardinia, Italy. The xenoliths originated from the underplating of variably evolved subduction-related basaltic liquids, which underwent cooling and recrystallisation in the deep crust (T=850–900 °C, P=0.8–1.0 GPa). They consist of orthopyroxene+clinopyroxene+plagioclase porphyroclasts (An=50–66 mol%) in a granoblastic, recrystallised, quartz-free matrix composed of pyroxene+plagioclase (An=56–72 mol%)+Fe–Ti oxides±K-feldspar±biotite±fluorapatite±Ti-biotite. Texturally, the K-feldspar occurs in a variety of different modes. These include: (1) rods, blebs, and irregular patches in a random scattering of plagioclase grains in the form of antiperthite; (2) micro-veins along plagioclase–plagioclase and plagioclase–pyroxene grain rims; (3) myrmekite-like intergrowths with Ca-rich plagioclase along plagioclase–plagioclase grain boundaries; and (4) discrete anhedral grains (sometimes microperthitic). The composition of each type of K-feldspar is characterized by relatively high albite contents (16–33 mol%). An increasing anorthite content in the plagioclase towards the contact with the K-feldspar micro-vein and myrmekite-like intergrowths into the K-feldspar along the plagioclase–K-feldspar grain boundary are also observed. Small amounts of biotite (TiO_2=4.7–6.5 wt.%; F=0.24–1.19 wt.%; Cl=0.04–0.20 wt.%) in textural equilibrium with the granulite-facies assemblage is present in both K-feldspar-bearing and K-feldspar-free xenoliths. These K-feldspar textures suggest a likely metasomatic origin due to solid-state infiltration of KCl-rich fluids/melts. The presence of such fluids is supported by the fluorapatite in these xenoliths, which is enriched in Cl (Cl=6–50% of the total F+Cl+OH). These lines of evidence suggest that formation of K-feldspar in the mafic xenoliths reflects metasomatic processes, requiring an external K-rich fluid source, which operated in the lower crust during and after in-situ high-T recrystallisation of relatively dry rocks.

Keywords: Granulite mafic xenoliths; Lower crust; Potassic (KCl) metasomatism; Sardinia

1. Introduction

Mafic and ultramafic xenoliths in alkaline volcanic rocks are generally thought to represent current samples of inaccessible upper mantle and lower crustal lithologies. In particular, granulite-facies xenoliths, which have been brought quickly to the surface by volcanic eruptions, are a unique source of information on the nature and processes active in the present-day lower, continental crust. Concurrently, there are obvious limitations to a thorough knowledge of the source area of the xenoliths, given the random

* Corresponding author. Tel.: +39 0521 905342; fax: +39 0521 905305.
E-mail address: alessandra.montanini@unipr.it (A. Montanini).

0024-4937/$ - see front matter © 2006 Elsevier B.V. All rights reserved.
doi:10.1016/j.lithos.2006.03.053

nature of their sampling by the host magmas, their typically small size, and the general lack of a mesoscopic relationship between different lithologies. In contrast, however, unambiguously recognized lower crustal terrains emplaced by tectonic processes are relatively rare (e.g., Mezger, 1992; Percival et al., 1992) and are usually characterized by retrograde metamorphism as well as deformation related to their exhumation history.

Several previous studies have been published on different occurrences of lower crustal xenoliths in Northern and Central Europe (see the reviews of Griffin and O'Reilly, 1987; Downes, 1993). These include regions unaffected by Alpine orogenic events and characterized by crustal domains consolidated both during Precambrian (e.g., East European Craton, NW Scotland) and Phanerozoic times (e.g. French Central Massif, North Hessian Depression, or Eifel, Ireland). Considerable advances in the knowledge of the lower crust beneath these regions have been achieved in the last decades through petrological and geophysical studies of their xenoliths. In contrast, samples from the present-day lower crust beneath Alpine Europe are extremely rare. Subsequently, the age and composition of this lower crust are poorly known, with the exception of the Pannonian Basin in Hungary (e.g. Kempton et al., 1997; Embey-Isztin et al., 2003). In addition, while convergent margins are well assessed to be a major site of lower crustal accretion through different mechanisms including basaltic underplating at the base of the crust and subduction–accretion (Kay and Kay, 1984; Weber et al., 2002 and references therein), very few examples of lower crustal xenoliths coming from active continental margins have been reported on (e.g. Selverstone and Stern, 1983; Kempton et al., 1997; Weber et al., 2002).

One example of lower crust that includes both Hercynian Europe as well as lying along an active continental margin can be found beneath the island of Sardinia. Here, mantle xenoliths are common in many of the Pliocene alkaline volcanics covering the island and, subsequently, have been extensively studied (e.g. Dostal and Capedri, 1976; de Albuquerque et al., 1977; Beccaluva et al., 1989, 2001). In contrast, only a few granulite-facies mafic xenolith studies exist of the lower crust beneath Sardinia (e.g. Rutter, 1987; Beccaluva et al., 1989). Consequently, in order to assess compositional and mineralogic variability of the present-day lower crust beneath an active continental margin, as well as to understand both lower crust formation and evolution, we present mineralogical and geochemical data for selected samples from a suite of 42 granulite-facies metagabbronorite xenoliths enclosed in basanite flows of Pliocene age from Western Sardinia. Remarkably, these mafic rocks commonly contain small amounts of K-feldspar and apatite, whose textural and compositional characters will be discussed and interpreted as evidence of KCl brine metasomatism operating in the lower crust.

2. Regional geology, sample localities, and host rock description

The Sardinia crystalline basement consists of Late Precambrian and Palaeozoic rocks (Carmignani et al., 1994) (Fig. 1). The western part of the crystalline basement is buried under a thick cover of Cenozoic volcanic and sedimentary rocks. The crystalline basement represents a segment of the southern European Hercynian chain and is composed of coalescent granitoid plutons and metamorphic terrains. The metamorphic terrains are characterized by a progressively increasing grade from SW (non-metamorphic/subgreenschist) to NE (amphibolite-facies rocks, migmatites and rare eclogitic relics). No granulite-facies rocks are exposed. Structural evidence, as well as stratigraphic and lithologic similarities, indicates that the Sardinian crystalline basement was linked to the Provencal and Massif Central basement at the end of the Hercynian cycle.

During the Mesozoic and Paleocene, Sardinia was part of the southern margin of the European plate sharing the geological history of the Iberian peninsula—Southern France up to Burdigalian, when anticlockwise rotation and formation of the Provencal Basin began (Montigny et al., 1981; Speranza et al., 2002). Starting in the late Oligocene, Sardinia become part of a rift system extending from Germany to Northern Spain (Lecca et al., 1997; Monaghan, 2001; Fig. 1). Extensional tectonics was associated with volcanic activity ranging in age between 32 and 13 Ma (Savelli et al., 1979; Beccaluva et al., 1985) that was related to the formation of NNW-dipping subduction zone off the present eastern coast of the island (Fig. 1). Volcanic rocks included large volumes of silicic lavas and pyroclastics with a calc-alkaline affinity, high-K calc-alkaline andesites, high-alumina basalts, and arc tholeiites (Coulon, 1977; Dostal et al., 1982; Assorgia et al., 1995; Lecca et al., 1997; Morra et al., 1997; Downes et al., 2001), all related to northwest-directed subduction of oceanic lithosphere of the Western Tethys. Eastward retreat of the Adria plate finally induced counter-clockwise rotation and separation of Sardinia (along with Corsica) from southern Europe, most probably between 19 and 16 Ma (Speranza et al., 2002).

In this complex tectonic framework a new volcanic phase took place in Western Sardinia between ca. 5.0 and 0.1 Ma (Beccaluva et al., 1985). These Pliocene–Pleistocene volcanics consist of mafic and differentiated rocks belonging to alkaline, transitional and tholeiitic series and were erupted in a within-plate extensional setting

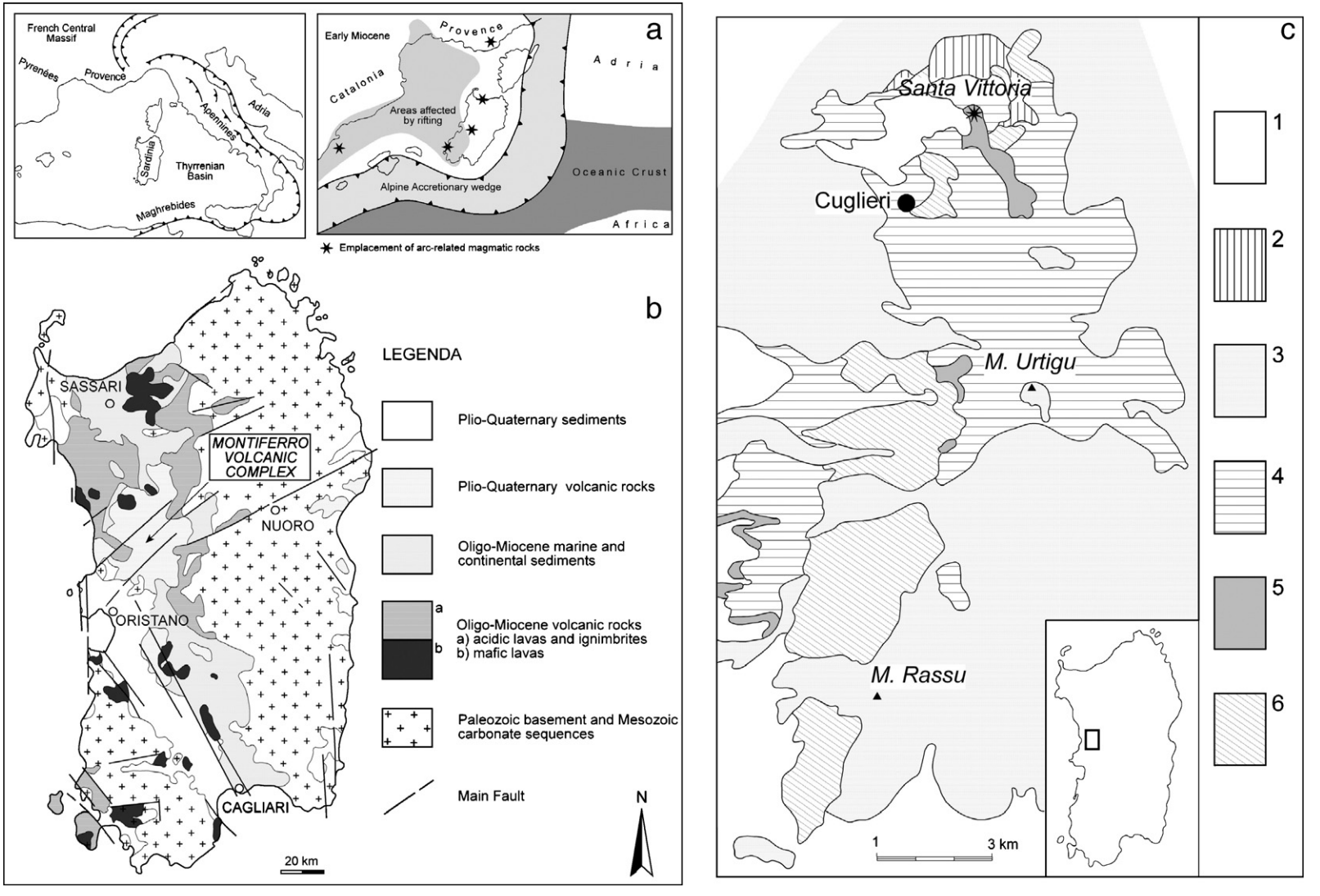

Fig. 1. (a) Simplified structural sketch and paleogeographic reconstruction of the Western Mediterranean area during Early Miocene (after Lecca et al., 1997); (b) geologic map of Sardinia showing the extent of the Oligocene–Miocene and Pliocene-Quaternary volcanism; (c) geologic sketch map of the Montiferro volcanic complex (1: quaternary sediments, 2: upper basanites, 3: phonolites and trachytes, 4: basalts, 5: lower basanites, 6: Oligo-Miocene calc-alkaline volcanic rocks, modified after Di Battistini et al., 1990) and xenolith sampling locality (asterisk).

(Beccaluva et al., 1977; Lustrino et al., 2002). The volcanic rocks from this period contain both ultramafic along with minor granulite-facies mafic xenoliths. The granulite-facies xenoliths, i.e. spinel-rich metagabbros (Montanini et al., 1992) and the metagabbronorites of this study, are well represented only in basanitic lavas from the Montiferro volcanic complex, which has been one of the most active sites of Tertiary volcanic activity in Sardinia. Felsic lithologies are completely absent among the xenoliths. The Montiferro products consist of (i) calc-alkaline lava flows and pyroclastics belonging to the older Oligo-Miocene volcanism (Gallo et al., 1974) and (ii) lava flows of Pliocene age with dominantly alkaline affinity (Beccaluva et al., 1977; Di Battistini et al., 1990).

The metagabbronorite xenoliths are enclosed in basanitic lava flows occurring at the base of the Montiferro volcanic succession ("Lower Basanites", Fig 1). Other associated xenoliths consist of mica megacrysts and rare phlogopite–(±amphibole)-bearing pyroxenites with igneous textures that indicate they likely crystallized from the basanitic magma at depth. Peridotite xenoliths are absent. The host basanitic lavas, erupted around 3.9 Ma (Beccaluva et al., 1985), contain olivine + clinopyroxene + Ti-rich phlogopite phenocrysts in a groundmass composed of plagioclase + clinopyroxene + olivine + globular analcite and minor amounts of micas, Fe–Ti oxides, K-feldspar and fluorapatite.

3. Analytical techniques

3.1. Electron microprobe analysis

Electron microprobe (EMP) analyses of pyroxenes, feldspars, amphibole, and oxides were carried out using a JEOL-6400 electron microprobe, equipped with Oxford Instruments ISIS energy-dispersive microanalytic system at the University of Parma, and a JEOL JXA-8600 electron microprobe, equipped with a Tracor Northern Series II 5600 wavelength-dispersive analytical system, at the IGG-CNR Institute in Florence. In the case of the JEOL-6400, operating conditions were 15 kV accelerating voltage, 0.62 nA current, a spot diameter of 1–2 μm, and counting time of 100 s. Biotite analyses were obtained on the JEOL JXA-8600. Here analytical conditions consisted of 15 kV accelerating voltage and a beam current of 0.20 nA. In both cases, synthetic and natural mineral standards were used for the calibration.

Apatite analyses as well as additional biotite and feldspar analyses were obtained on the CAMECA SX50 and SX100 at the GeoForschungsZentrum Potsdam. Analytical conditions for the silicates consisted of a 15 kV acceleration voltage, 20 nA beam current, and counting times of 10–30 s depending on the element. Beam spot size was 5 μm for biotite and amphibole and 15 μm for feldspar and fluorapatite. Silicate and oxide standards were taken from both the CAMECA and Smithsonian standard sets (Jarosewich et al., 1980). The CAMECA PAP program was used for matrix correction (Pouchou and Pichoir, 1985). For fluorapatite, counting times were 20 to 120 s depending on the relative amount of the element. Technique and counting times for (Y + REE) are described in Harlov et al. (2002). Standards for the REE were taken from synthetic REE phosphates prepared by Jarosewich and Boatner (1991), with the remaining standards taken from the Durango fluorapatite and the Smithsonian oxide and silicate standard set (Jarosewich et al., 1980). EMP measurement of Cl and F in fluorapatite were made according to guidelines outlined in Stormer et al. (1993). For all analyses, unless otherwise specified, only mineral cores were analysed and mineral rims avoided. Feldspar, pyroxene and fluorapatite analyses are contained in Tables 1, 2 and 4, respectively whereas both biotite and amphibole analyses are contained in Table 3.

3.2. Whole-rock analysis

Whole-rock chemical analyses were obtained after carefully removing the margins of the metagabbronorite xenoliths by sawing in order to reduce possible infiltration effects by the host basanite magma. Major and trace (Ni, Co, Cr, V, Sc, Cu, Zn, Ga) elements were determined by conventional X-ray fluorescence (XRF) techniques at the University of Parma. Rare earth elements (REE), U, Th, Cs, Rb, Ba, Sr, Zr, Nb, Y, Ta, and Hf abundances were determined by ICP-MS spectrometry at "Activation Laboratories" (Ancaster, Ontario). Precision and accuracy of XRF and ICP trace element analyses are usually within 5–10%. Whole-rock analyses are contained in Table 5.

4. Xenolith petrology, mineralogy and whole-rock chemistry

4.1. Petrography and mineral chemistry

The metagabbronorite xenoliths are sub-rounded fragments with diameters ranging between 5 and 15 cm. They are medium-grained rocks with variable degrees of recrystallisation and deformation. Examination of 42 metagabbronorite xenoliths in thin section indicate that textures vary from nearly isotropic (predominantly granoblastic with straight grain boundaries) to foliated. Deformed rocks display a discontinuous foliation defined by lenticular plagioclase- and pyroxene-rich domains. They consist of plagioclase (64–27 vol.%), clinopyroxene (15–39

Table 1
Representative EMP analyses (wt.%) of orthopyroxene and clinopyroxene

		SiO_2	TiO_2	Al_2O_3	Cr_2O_3	FeO	MnO	MgO	CaO	Na_2O	Sum
NB6	Opx	52.50	0.00	3.08	0.00	18.40	0.64	24.00	0.58	–	99.20
	Cpx	51.60	0.65	3.26	0.31	7.66	0.00	14.60	20.60	0.51	99.19
NB7	Opx	52.62	0.00	1.76	0.05	21.31	0.51	22.88	0.53	–	99.65
		0.35	*0.00*	*0.21*	*0.07*	*0.24*	*0.07*	*0.32*	*0.07*	*0.00*	
	Cpx	51.34	0.52	3.68	0.15	8.93	0.20	13.23	20.90	0.86	99.81
		0.37	*0.08*	*0.31*	*0.13*	*0.30*	*0.10*	*0.38*	*0.56*	*0.10*	
	Cpx-p–c	50.60	0.66	4.14	0.26	8.93	0.21	13.00	20.80	0.88	99.70
	Cpx-p–r	51.80	0.46	3.02	0.15	8.86	0.00	13.50	21.50	0.66	100.08
	Cpx-n	51.50	0.46	3.74	0.00	8.94	0.28	13.57	20.43	0.92	100.04
		0.20	*0.07*	*0.02*	*0.00*	*0.57*	*0.03*	*0.15*	*0.65*	*0.09*	*0.06*
NB8	Opx	52.30	0.12	1.88	0.11	22.90	0.49	20.93	0.75	–	99.48
		0.98	*0.12*	*0.23*	*0.10*	*1.23*	*0.08*	*0.23*	*0.11*		
	Cpx	51.28	0.45	3.41	0.08	10.38	0.25	12.75	20.48	0.93	100.01
		0.22	*0.09*	*0.15*	*0.11*	*0.43*	*0.20*	*0.39*	*0.43*	*0.05*	
NB271	Opx	51.60	0.00	1.12	0.00	24.60	0.88	20.10	0.65	–	98.95
		0.14		*0.06*		*0.28*	*0.12*	*0.14*	*0.03*		
	Cpx	51.48	0.06	2.34	0.00	10.46	0.33	12.82	21.32	0.88	99.69
		0.20	*0.14*	*0.16*		*0.26*	*0.06*	*0.13*	*0.16*	*0.04*	
NB313	Opx	51.85	0.06	2.74	0.04	21.70	0.51	22.60	0.60	0.01	100.11
		0.07	*0.08*	*0.11*	*0.03*	*0.42*	*0.02*	*0.14*	*0.02*	*0.01*	
	Cpx	50.15	0.62	4.79	0.03	9.84	0.29	12.65	21.70	0.71	100.78
		0.21	*0.03*	*0.22*	*0.04*	*0.08*	*0.05*	*0.07*	*0.57*	*0.08*	
NB316	Opx	53.40	0.05	1.90	0.20	17.58	0.37	25.47	0.48	–	99.45
		0.13	*0.08*	*0.15*	*0.14*	*0.28*	*0.11*	*0.08*	*0.02*		
	Cpx	52.08	0.44	3.43	0.26	6.62	0.09	14.22	21.80	0.92	99.86
		0.58	*0.13*	*0.29*	*0.10*	*0.57*	*0.10*	*0.26*	*0.16*	*0.23*	
NB318	Opx	51.98	0.14	1.87	0.09	21.38	0.54	23.35	0.59	–	99.94
		0.29	*0.03*	*0.07*	*0.09*	*0.30*	*0.05*	*0.31*	*0.04*		
	Cpx	51.35	0.33	3.30	0.07	8.72	0.19	13.60	22.10	0.88	100.54
		0.21	*0.24*	*0.47*	*0.10*	*0.59*	*0.01*	*0.57*	*0.28*	*0.26*	
NB321	Opx	53.10	0.00	2.61	0.15	18.15	0.53	24.60	0.63	–	99.77
		0.14		*0.33*	*0.21*	*0.21*	*0.13*	*0.01*	*0.08*		
	Cpx	52.28	0.36	3.88	0.11	7.08	0.28	14.28	20.68	0.76	99.71
		0.39	*0.26*	*0.43*	*0.14*	*0.70*	*0.21*	*0.62*	*0.43*	*0.08*	
NB323	Opx	52.30	0.10	3.40	0.20	18.20	0.46	24.40	0.57	–	99.63
		0.14	*0.14*	*0.06*	*0.06*	*0.42*	*0.13*	*0.28*	*0.23*		
	Cpx	51.40	0.55	4.97	0.00	7.14	0.00	14.10	20.33	0.93	99.42
		0.72	*0.23*	*0.53*		*0.45*		*0.52*	*0.50*	*0.36*	
	Cpx-p–c	50.60	0.81	5.55	0.00	7.43	0.00	13.80	20.40	0.60	99.19
	Cpx-p–r	52.00	0.47	4.86	0.00	7.37	0.00	13.80	19.80	1.31	99.70
NB324	Opx	51.43	0.07	2.24	0.00	25.03	0.56	20.20	0.73	–	100.26
		0.38	*0.12*	*0.29*		*0.67*	*0.09*	*0.44*	*0.04*		
	Cpx	50.50	0.51	3.79	0.00	11.00	0.21	12.30	20.70	0.40	99.41
NB 331	Opx	51.45	0.00	2.88	0.00	23.35	0.49	20.90	0.88	–	99.95
		0.49		*0.73*		*1.34*	*0.08*	*0.71*	*0.21*		
	Cpx	50.75	0.37	3.96	0.04	11.60	0.25	12.25	19.75	0.77	99.74
		0.21	*0.06*	*0.13*	*0.06*	*0.57*	*0.06*	*0.07*	*0.92*	*0.01*	

(–) not analized; italics values are standard deviations; p = porphyroclast, n = neoblast, c = core, r = rim.

vol.%), orthopyroxene (12–36 vol.%), Fe–Ti oxides (1–8 vol.%)±biotite (≤6 vol.%)±brown amphibole± K-feldspar±olivine±yellow-orange fluorapatite±green spinel.

The metagabbronorite xenoliths are commonly characterized by relatively large (up to 8–10 mm in length) porphyroclasts of orthopyroxene (and more rarely, clinopyroxene) in a granoblastic, recrystallised matrix principally composed of pyroxenes, plagioclase, and Fe–Ti oxides (Fig. 2a). The pyroxene porphyroclasts display well developed mutual exsolution lamellae and blebs. They may show evidence of plastic deformation, i.e. bending, kinking and undulose extinction. In places, plagioclase occurs as large subhedral grains with undulose extinction

Table 2
Representative EMP analyses (wt.%) of biotite and amphibole

		SiO_2	TiO_2	Al_2O_3	Cr_2O_3	FeOt	MnO	MgO	CaO	BaO	K_2O	Na_2O	H_2O*	F	Cl	Sum	O=F	O=Cl	Total
NB313	Bt	36.70	4.82	15.53	0.08	15.40	0.11	13.60	0.10	–	10.02	0.64		–	–				
		0.60	*0.13*	*0.31*	*0.08*	*0.53*	*0.13*	*0.53*	*0.13*	–	*0.53*	*0.19*							
NB316	Bt	37.53	6.05	15.28	0.42	11.94	0.07	15.11	0.13	0.24	9.08	0.52	3.76	0.51	0.06	100.69	0.21	0.01	100.47
		0.61	*0.33*	*0.89*	*0.06*	*0.73*	*0.03*	*0.46*	*0.25*	*0.02*	*0.77*	*0.19*	*0.18*	*0.34*	*0.01*				
NB318	Bt	37.04	4.99	15.07	0.22	14.76	0.04	14.27	0.07	0.17	9.67	0.50	3.62	0.65	0.13	101.19	0.27	0.03	100.89
		0.29	*0.11*	*0.22*	*0.03*	*0.41*	*0.03*	*0.13*	*0.09*	*0.04*	*0.52*	*0.23*	*0.14*	*0.25*	*0.06*				
NB321	Bt	37.04	6.08	15.23	0.37	13.40	0.04	14.21	0.08	0.44	9.44	0.47	3.87	0.19	0.02	100.88	0.08	–	100.79
		0.44	*0.40*	*0.79*	*0.09*	*0.83*	*0.04*	*0.42*	*0.08*	*0.06*	*0.07*	*0.27*	*0.05*	*0.08*	*0.00*				
NB322	Bt	37.96	5.14	14.77	0.21	13.82	0.05	15.81	0.31	0.11	8.77	0.67	3.61	1.07	0.08	102.39	0.45	0.02	101.92
		0.32	*0.51*	*0.10*	*0.01*	*0.24*	*0.00*	*0.29*	*0.32*	*0.01*	*0.34*	*0.05*	*0.35*	*0.70*	*0.01*				
NB323	Bt	37.71	6.28	14.37	0.21	15.09	0.04	13.11	0.08	0.52	9.99	0.18		–	–				
		0.61	*0.34*	*0.55*	*0.16*	*0.24*	*0.06*	*0.49*	*0.07*	*0.16*	*0.23*	*0.10*		–	–				
	Amph	40.40	3.54	12.19	n.d.	14.13	0.18	12.71	12.10		1.39	1.71		0.42	0.07	98.80			
		0.28	*0.35*	*0.65*		*0.25*	*0.03*	*0.29*	*0.07*		*0.01*	*0.21*		–	–				
NB325	Bt	38.51	5.25	15.48	0.19	13.63	0.05	14.70	0.03	0.20	9.34	0.46	4.00	0.30	0.04	102.18	0.13	0.01	102.05
		0.24	*0.32*	*0.35*	*0.04*	*0.37*	*0.01*	*0.25*	*0.02*	*0.01*	*0.15*	*0.03*	*0.16*	*0.33*	*0.01*				

Blank = below EMP detection limit; italics values are standard deviations.
* calculated assuming that the site (Cl,F,OH) is filled.

and curved multiple twins. The pyroxene porphyroclasts and the former plagioclase can be viewed as textural relics of the original igneous assemblage. Olivine has been found only in two out of 42 samples examined in thin section. It occurs as irregular-shaped crystals included into orthopyroxene or as small polygonal grains included into domains of recrystallized pyroxenes. Symplectitic intergrowths of clinopyroxene+orthopyroxene+green spinel in contact with plagioclase (Fig. 2b) likely represent a reaction between plagioclase and former olivine.

Strongly pleochroic, reddish-brown to yellow-brown biotite is present as small (<1 mm) flakes and lamellae parallel to the foliation (Fig. 2c) or, less commonly, as larger crystals of irregular shape. Brown amphibole, coexisting with biotite, is rare and occurs as crystals with straight boundaries forming 120° triple junctions with adjacent granulite-facies minerals. Fe–Ti oxides usually form small polygonal grains and, rarely, interstitial crystals or subhedral grains enclosed into pyroxenes and plagioclase. Small amounts (from traces up to ca. 2 vol. %) of K-feldspar have been observed in about half of the examined xenoliths (see Section 4.2.).

No apparent infiltration of basanitic melt or hydrothermal alteration have been found in the metagabbronorite xenoliths. However, mineralogical transformations due to heating and, possibly, also to reaction with the host magma have been observed in some samples. Primary olivine is completely converted to dark red-orange iddingsitic products. Orthopyroxene may show opaque oxidized rims (e.g. Selverstone and Stern, 1983) or, more rarely, coronas made up of secondary olivine+clinopyroxene+K-feldspar. Biotite locally breaks down to fine-grained K-feldspar+ilmenite + orthopyroxene, but most micas are stable or show only thin opaque rims. Amphibole is largely replaced by cryptocrystalline semi-opaque aggregates.

Pyroxenes (Table 1) can be classified as ferroan diopside and ferroan enstatite according to IMA classification system (Rock, 1990). Both porphyroclastic and neoblastic pyroxenes have low TiO_2 (0.3–0.6% in clinopyroxene, negligible in orthopyroxene) and moderate Al_2O_3 (4.9–2.4 wt.% in clinopyroxene, 3.4–1.9% in orthopyroxene) and Cr_2O_3 ($\leq$0.3%) contents. Mg# (=100 Mg/(Mg+Fe^{2+})) varies between 81.7–64.6 and 78.2–58.5 for clino- and orthopyroxene, respectively. The restricted solid solution between Ca-poor and Ca-rich pyroxenes, as shown by the low CaO content of orthopyroxene (0.4–0.8 wt.%) indicates slow cooling from magmatic temperatures. The Al^{VI}/Al^{IV} ratios of the clinopyroxenes are typical of granulite-facies xenoliths according to the classification system of Aoki and Kushiro (1968). Both pyroxenes show a moderate trend of enrichment in Fe into the pyroxene quadrilateral (not shown). A slight core-to-rim Al

Table 3
EMP analyses (wt.%) of fluorapatite

Sample		P_2O_5	SiO_2	SO_3	Y_2O_3	La_2O_3	Ce_2O_3	Nd_2O_3	Sm_2O_3	Gd_2O_3	Dy_2O_3	CaO	MnO	FeO*	SrO	Na_2O	F	Cl	H_2O#	Sum	O=(F+Cl)	Total	$(Y+REE)_2O_3$
NB 6	FAp 1	40.65	0.12	0.09		0.06	0.18	0.04	0.04	0.05	0.02	54.92	0.06	0.27	0.06	0.05	2.20	0.30	1.21	100.31	−1.00	99.32	0.38
		0.41	*0.02*	*0.01*		*0.03*	*0.01*	*0.02*	*0.01*	*0.01*	*0.01*	*0.10*	*0.00*	*0.10*	*0.01*	*0.04*	*0.21*	*0.03*					
	FAp 2	40.72	0.12	0.11		0.03	0.18					54.73	0.04	0.42	0.05	0.12	3.10	0.26	0.38	100.26	−1.36	98.90	0.21
NB 8	FAp 1	40.41	0.17	0.02	0.03	0.10	0.24	0.11	0.06	0.06	0.07	53.85	0.07	0.56	0.06	0.08	2.13	0.69	1.07	99.77	−1.05	98.72	0.67
		0.14	*0.01*	*0.01*	*0.01*	*0.03*	*0.04*	*0.05*	*0.05*	*0.05*	*0.04*	*0.22*	*0.01*	*0.08*	*0.01*	*0.02*	*0.24*	*0.03*					
	FAp 2	40.71	0.18	0.01		0.12	0.33	0.18			0.04	53.95	0.08	0.65	0.06	0.05	2.15	0.36	1.25	100.08	−0.98	99.10	0.66
NB12		41.55	0.16	0.06	0.01	0.08	0.24	0.11	0.07	0.03	0.03	54.71	0.03	0.15	0.04	0.09	2.44	0.41	1.01	101.23	−1.12	100.11	
		0.37	*0.02*	*0.02*	*0.01*	*0.04*	*0.09*	*0.05*	*0.03*	*0.02*	*0.03*	*0.20*	*0.02*	*0.03*	*0.03*	*0.03*	*0.21*	*0.05*					
NB 322	FAp 1	40.40	0.20	0.08	0.01	0.12	0.27	0.14	0.02	0.08	0.05	53.99	0.04	0.27	0.03	0.10	2.24	0.66	0.98	99.68	−1.09	98.59	0.69
		0.26	*0.02*	*0.01*	*0.00*	*0.02*	*0.03*	*0.04*	*0.01*	*0.01*	*0.03*	*0.10*	*0.01*	*0.14*	*0.01*	*0.02*	*0.08*	*0.03*					
	FAp 2	40.36	0.18	0.10		0.03	0.20	0.10	0.01		0.05	54.24	0.03	0.16	0.04	0.09	1.91	0.73	1.24	99.49	−0.97	98.52	0.39
	FAp 3	40.27	0.17	0.06		0.09	0.19	0.09	0.04	0.06	0.05	54.01	0.04	0.21	0.05	0.11	2.66	0.57	0.62	99.28	−1.25	98.03	0.52
	FAp 4	40.63	0.21	0.09	0.01	0.16	0.26	0.08	0.06	0.07	0.02	54.30	0.04	0.19	0.03	0.08	3.24	0.33	0.22	100.00	−1.44	98.57	0.65
		0.17	*0.02*	*0.02*	*0.00*	*0.01*	*0.03*	*0.03*	*0.01*	*0.05*	*0.00*	*0.19*	*0.00*	*0.04*	*0.00*	*0.00*	*0.15*	*0.05*					
NB 324	FAp 1	40.51	0.16	0.02	0.03	0.08	0.16	0.11	0.07	0.05	0.04	54.29	0.09	0.61	0.02	0.20	1.97	0.46	1.34	100.21	−0.93	99.28	0.53
	FAp 2	40.45	0.16	0.02	0.03	0.04	0.24	0.12	0.09	0.06	0.03	54.14	0.05	0.46	0.04	0.16	2.27	0.45	1.05	99.85	−1.06	98.79	0.60
	FAp 3	40.74	0.16	0.06	0.02	0.12	0.17	0.11	0.04	0.04	0.02	54.34	0.06	0.32	0.05	0.12	1.67	0.50	1.62	100.16	−0.82	99.34	0.52
NB 325		40.60	0.18	0.07	0.02	0.09	0.18	0.09	0.05	0.04	0.02	54.43	0.04	0.26	0.05	0.08	1.71	0.39	1.63	99.92	−0.81	99.12	0.40
		0.10	*0.04*	*0.01*	*0.01*	*0.02*	*0.04*	*0.03*	*0.01*	*0.02*	*0.01*	*0.40*	*0.01*	*0.05*	*0.01*	*0.02*	*0.11*	*0.02*					
NB 331		40.24	0.39	0.04	0.02	0.06	0.15	0.09		0.02	0.04	54.00	0.12	0.68	0.04	0.16	1.66	1.46	1.19	100.36	−1.03	99.33	0.39

Blank = below EMP detection limit.
* total Fe as FeO. # calculated by charge balance.

depletion, sometimes accompanied by an increase in Na, is observed in the clinopyroxene porphyroclasts. A similar Al decrease is recorded by the recrystallized clinopyroxenes (Table 1).

Biotite is Mg-(Mg#=71.6–63.3) and Ti-rich (TiO_2= 4.7–6.3 wt.%) (Table 2). Such elevated TiO_2 contents greatly enhance the biotite thermal stability under high-*T* granulite-facies conditions (Patiño Douce, 1993). Low

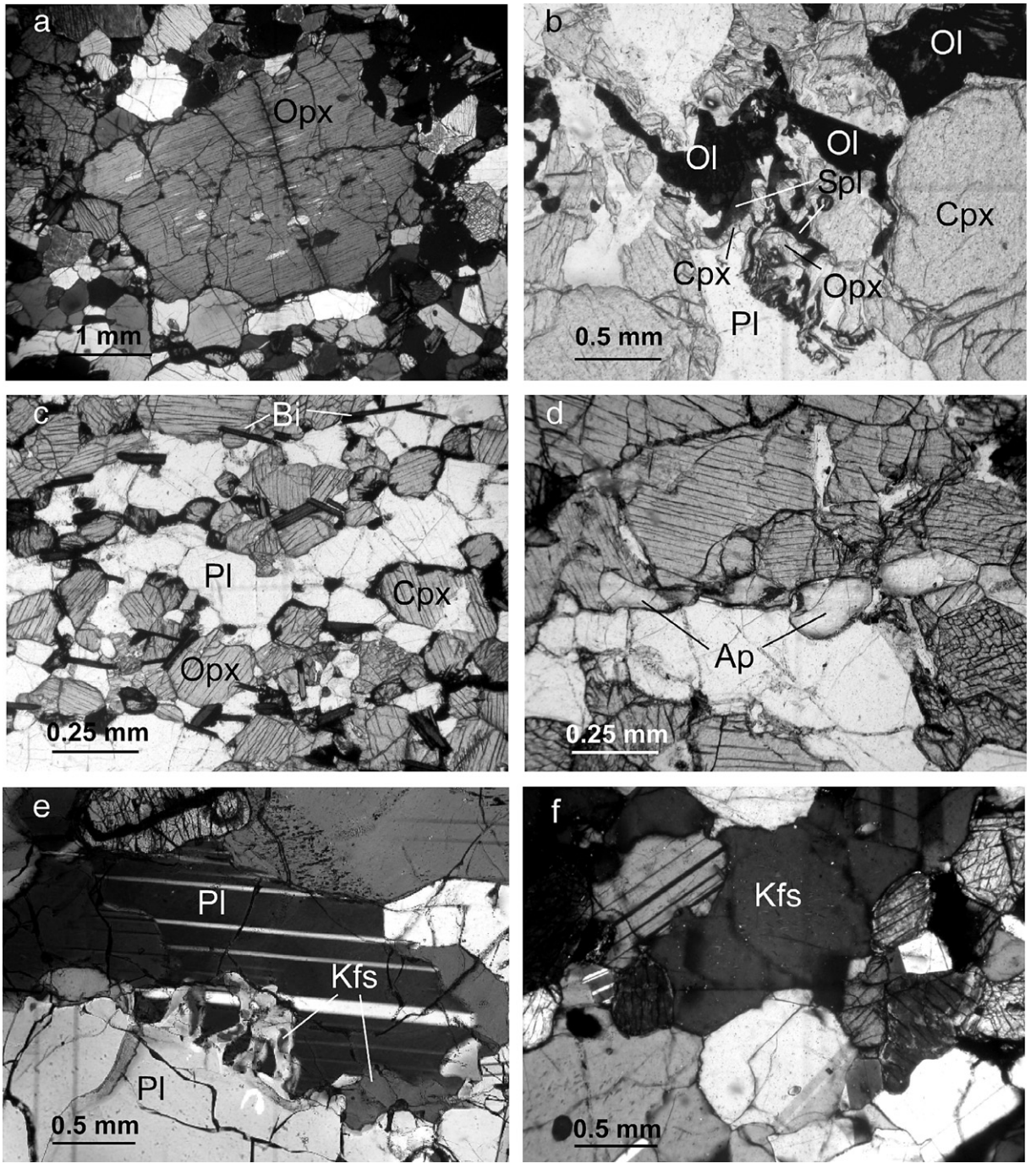

Fig. 2. Photomicrographs of the metagabbronorite textures. (a) orthopyroxene porphyroclast with clinopyroxene exsolution lamellae and blebs; (b) primary olivine (dark, completely iddingsitized) showing development of pyroxene+Al-rich spinel rims and symplectitic intergrowths at the interface with plagioclase; (c) biotite flakes aligned along the granulitic foliation; (d) trail of small rounded to polygonal apatite grains, (e) myrmekite-like plagioclase–plagioclase intergrowths associated with K-feldspar (1) and incipient development of K-feldspar micro-vein (2); (f) discrete microperthitic K-feldspar.

Cl (0.04–0.20 wt.%) and low to moderate F (0.24–1.19 wt.%) have been observed.

Amphibole can be classified as Ti-pargasite (Table 2) according to the nomenclature of Leake et al. (1997).

Fe–Ti oxides consist of magnetite, sometimes relatively Cr-rich (Cr_2O_3 up to ~3 wt.%), and ilmenite, whereas the occurrence of Al-rich Cr-poor hercynitic spinel is restricted to the olivine-plagioclase reaction zones.

Fluorapatite (Fig. 2d) is a common accessory mineral in 10 of the 42 metagabbro xenoliths included in this study (Table 3). Transmitted light microscopy, as well as back scattered electron (BSE) imaging, indicate that fluorapatite is completely free of inclusions. Generally, the fluorapatite grains show a variable F and Cl content per sample (Table 4). Fluorine and Cl contents in the fluorapatite range from 1.66 to 3.24 wt.% and 0.26 to 1.46 wt.%, respectively. These halogen content implies a calculated H_2O content ranging from 0.22 to 1.63 wt.% though this does not preclude the possibility that a portion, or perhaps all, of this presumed H_2O component consists a possible CO_2 component (cf. O'Reilly and Griffin, 2000).

4.2. Feldspar textures and composition

About half of the 42 metagabbronorite xenoliths examined are characterized by a series of peculiar feldspar textures associated with K-feldspar. These include:

(1) Antiperthite-like rods, blebs, and irregular patches of K-feldspar ($Ab_{24–29}Or_{78–72}An_{2–1}$) in a random scattering of plagioclase grains, (Fig. 3). An element line scan across one of these blebs indicates enrichment in Na in the plagioclase at the K-feldspar-plagioclase grain boundary interface followed by enrichment in Ca going outward into the plagioclase (Fig. 4).

Table 4
Representative EMP analyses (wt.%) of K-feldspar and plagioclase

		SiO_2	Al_2O_3	FeO	CaO	BaO	Na_2O	K_2O	Total
NB8	K-feldspar	65.49	18.68	0.13	0.42	0.50	2.29	12.76	100.26
		0.25	*0.15*	*0.03*	*0.04*	*0.15*	*0.24*	*0.38*	
	Plagioclase	53.51	29.15	0.27	12.39	0.01	4.13	0.69	100.14
		0.60	*0.20*	*0.05*	*0.22*	*0.01*	*0.10*	*0.06*	
	Diffuse brighter region in Plagioclase near K-feldspar	50.79	31.16	0.27	15.01	0.00	2.93	0.45	100.61
NB12	K-feldspar	66.11	18.71	0.04	0.19	0.39	2.40	12.73	100.57
		0.09	*0.02*	*0.01*	*0.01*	*0.00*	*0.27*	*0.40*	
	Plagioclase	55.32	28.64	0.16	11.53	0.01	4.81	0.53	101.00
		0.09	*0.07*	*0.01*	*0.02*	*0.01*	*0.02*	*0.01*	
NB271	Plagioclase	54.00	28.90	0.28	10.20	–	5.44	0.31	99.13
NB313	Plagioclase	50.30	31.97	0.31	13.67	–	3.14	0.24	99.63
		0.53	*0.47*	*0.16*	*0.59*		*0.41*	*0.08*	
	Plagioclase-p–c	50.70	31.60	0.27	13.00	–	3.62	0.24	99.43
	Plagioclase-p–r	49.70	32.50	0.18	13.90	–	2.89	0.32	99.49
	Plagioclase-n	50.50	31.80	0.49	14.10	–	2.92	0.17	99.98
NB321	Plagioclase	53.58	29.15	0.14	11.28	–	5.21	0.57	99.93
		0.22	*0.35*	*0.17*	*0.25*		*0.20*	*0.08*	
NB322	K-feldspar	65.96	18.73	0.05	0.21	0.37	2.35	12.94	100.60
		0.23	*0.04*	*0.00*	*0.02*	*0.03*	*0.26*	*0.29*	
	Plagioclase	55.31	28.49	0.17	11.32	0.01	4.87	0.56	100.74
		0.29	*0.01*	*0.01*	*0.10*	*0.00*	*0.02*	*0.01*	
NB323	Plagioclase	48.43	32.97	0.28	14.60	–	3.08	0.17	99.53
		0.48	*0.37*	*0.09*	*0.46*		*0.43*	*0.07*	
	Plagioclase-p–c	48.70	32.50	0.44	14.00	–	3.39	0.13	99.86
	Plagioclase-p–r	47.60	33.40	0.21	15.20	–	2.52	0.26	99.19
	Plagioclase-n	48.40	33.00	0.26	14.80	–	3.36	0.09	99.91
NB324	K-feldspar	66.39	19.03	0.18	0.38	0.60	3.67	10.81	101.06
		0.08	*0.02*	*0.01*	*0.00*	*0.06*	*0.10*	*0.15*	
	Plagioclase	55.48	28.71	0.27	11.55	0.02	4.74	0.72	101.49
		0.35	*0.22*	*0.01*	*0.29*	*0.00*	*0.10*	*0.03*	
	Diffuse brighter region in Plagioclase near K-feldspar	53.07	29.33	0.28	12.58	0.01	4.13	0.44	99.85
NB331	Plagioclase	51.70	30.80	0.35	12.60	–	3.79	0.34	99.58
		0.71	*0.57*	*0.09*	*0.28*	–	*0.16*	*0.13*	

(–) not analized; italics values are standard deviations; p = porphyroclast, n = neoblast, c = core, r = rim.

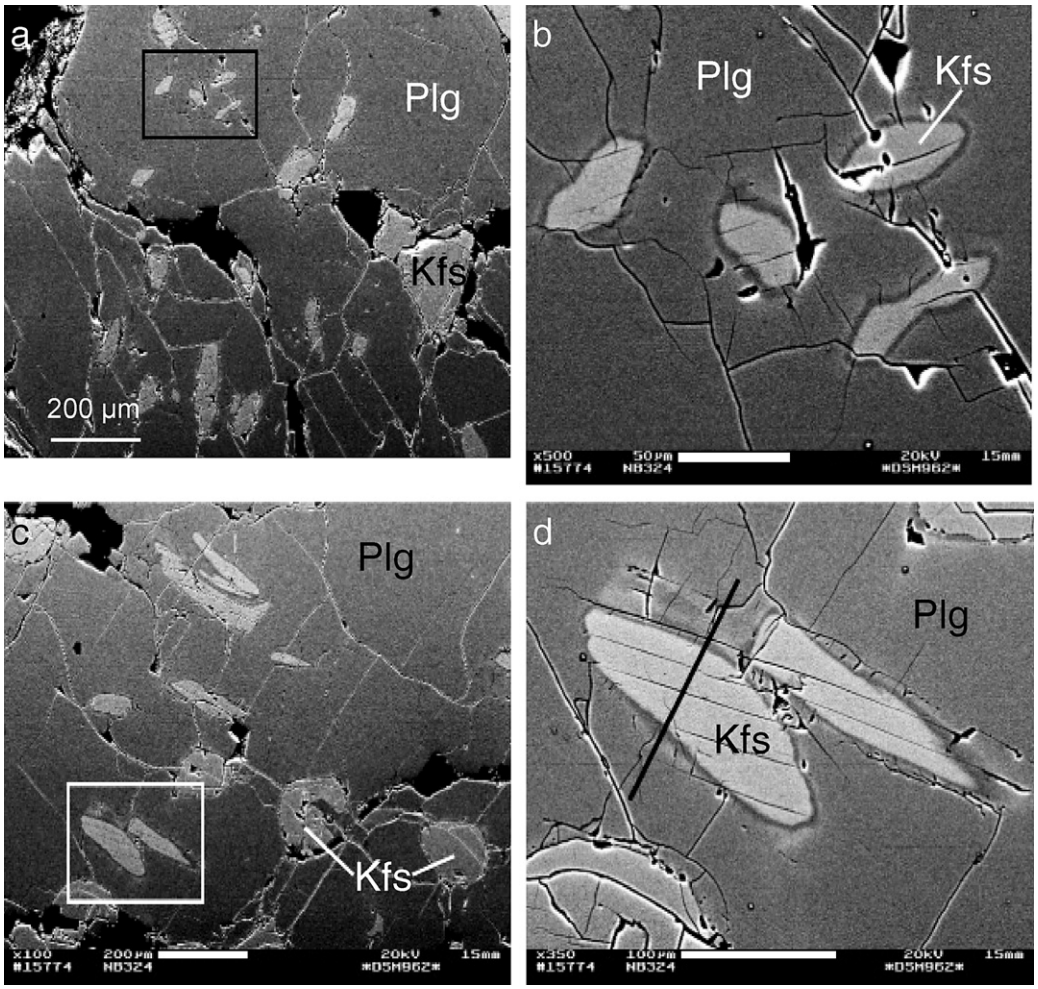

Fig. 3. BSE (back-scattered electron images) of replacement anti-perthite in plagioclase grains.

(2) Micro-veins of K-feldspar ($Ab_{11-33}Or_{84-65}An_{6-1}$) along plagioclase–plagioclase and plagioclase–pyroxene grain rims. These micro-veins sometimes show evidence of recrystallisation (Fig. 5).
(3) Myrmekite-like intergrowths of K-feldspar ($Ab_{17-28}Or_{82-67}An_{4-1}$) with plagioclase ($Ab_{37-45}Or_{5-8}An_{56-46}$) along plagioclase–plagioclase grain boundaries (Figs. 2e, and 6).
(4) Discrete anhedral grains of K-feldspar ($Ab_{16-23}Or_{82-75}An_{2-1}$) of which a random number of grains are microperthitic (Fig. 2f). This last texture is especially seen in the largest K-feldspar crystals, which are usually characterized by tiny elongate albite exsolutions.

The K-feldspar associated with the late coronas around orthopyroxene (see Section 4.1) is albite-rich ($Ab_{45-47}Or_{47-42}An_{5-1}$) and contains significant amounts of Ba (BaO up to 2.4 wt.%).

The plagioclase feldspars show a relatively wide range of compositions between An_{76} and An_{46}. Plagioclase porphyroclasts, in K-feldspar-free samples or in K-feldspar-bearing rocks far from the K-feldspar micro-veins, are usually characterized by a thin rim enriched in anorthite. Recrystallized plagioclase is also enriched in anorthite with respect to the plagioclase porphyroclast core (Table 2). The reverse zoning and Ca enrichment in neoblastic plagioclase is most likely related to granulite-facies recrystallization, suggesting a subsolidus equilibration at relatively high pressure, through a reaction between plagioclase and clinopyroxene: Albite (plagioclase)+Ca–Tschermak (clinopyroxene)=Jadeite (clinopyroxene)+ Anorthite (plagioclase) (see Kushiro, 1969; Kay and Kay, 1984; Rudnick and Taylor, 1987).

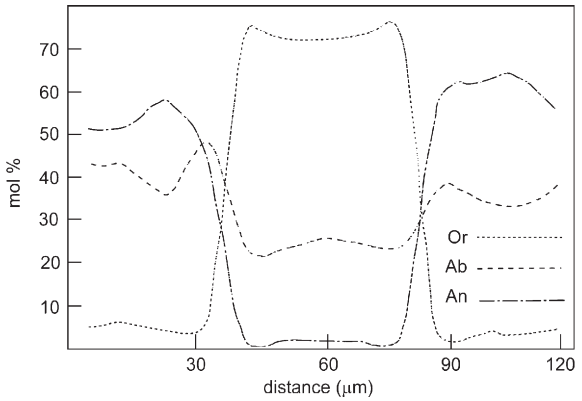

Fig. 4. Elemental line scans for Ab, Or and An across an exsolution lamella in replacement antiperthite (cf. Fig. 3d).

Plagioclase close to the K-feldspar micro-veins is usually slightly depleted in Na in a zone some tenths of a micron in width. Plagioclase intergrown with K-feldspar is relatively Na-rich, whereas Ca enrichment is observed in the plagioclase close to the intergrowths. This is in contrast to plagioclase close to the K-feldspar rods and blebs, in which enrichment in Na, coupled with depletion in Ca, is seen along a thin rim at the plagioclase–K-feldspar grain boundary interface (cf. Figs. 3b, d, and 4). This enrichment is contrasted with Na depletion in the plagioclase further away from the K-feldspar bleb. No zoning is observed in the plagioclase along the grain boundary interface with the largest discrete K-feldspar crystals though a slight enrichment in Na is seen.

4.3. Geochemistry of the metagabbronorite xenoliths and host rocks

The metagabbronorite xenoliths have predominantly basic (SiO_2 = 48.1–53.2 wt.%) compositions (Table 5). Most rocks are slightly oversaturated (normative quartz ≤ 3 wt.%); the only exceptions are the olivine-

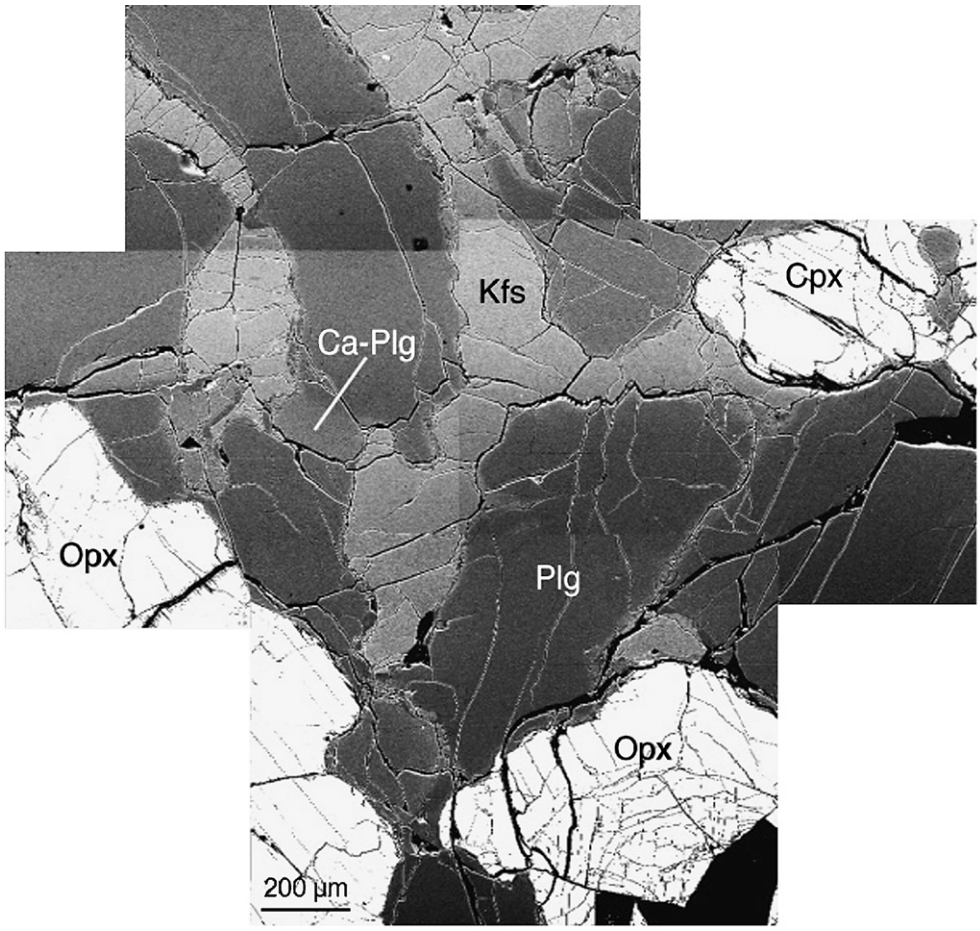

Fig. 5. BSE (back-scattered electron images) of micro-veins of apparently recrystallised K-feldspar along plagioclase–plagioclase and plagioclase–pyroxene grain rims. Note regions of Ca-enriched plagioclase associated with the K-feldspar micro-veins.

bearing sample NB312 and the low-silica, Fe–Ti oxide-rich sample NB271 that contain moderate amounts of normative olivine (7–8 wt.%). The xenoliths have a wide range of Mg#, i.e. 77–56, where Mg# = 100 Mg/(Mg + Fe^{2+}). Most samples have Mg# and SiO_2/Al_2O_3 values plotting within the field of primitive basaltic liquids (Fig. 7), thus excluding a significant role for cumulus processes in the origin of their protoliths.

The Mg# shows a positive correlation with compatible trace elements Ni (=240–20 ppm), Cr (970–8 ppm), Co (57–30 ppm) and a negative correlation with TiO_2 (0.33–1.28 wt.%), Al_2O_3 (12.1–20.1 wt.%), Na_2O (0.89–2.70 wt.%) and Sr (157–321 ppm) (Fig. 8). A tholeiitic enrichment trend in Fe is also seen in the AFM diagram (not reported). Incompatible minor and trace elements show low to moderate abundances (K_2O = 0.2–1.0 wt.%, Rb ≤ 24 ppm, Ba = 60–300 ppm, Y = 10–20 ppm, La ~ 14–60 ppm) and are not well correlated with a fractionation index like the Mg# or SiO_2 (Table 5). There is moderate LREE fractionation (La_N/Sm_N = 1.1–3.6) and LREE enrichment over HREE (La_N/Yb_N ~ 2–7), nearly flat HREE, and general absence of Eu anomaly or a slight enrichment in the samples with the lowest SiO_2/Al_2O_3 ratios (NB313, NB5) (Table 5; Fig. 9a). LILE-enrichment (with a peak at Ba) and prominent HFSE depletion are seen in the MORB-normalized patterns of the incompatible elements (Fig. 9b).

The basanitic host lavas (Table 5) are strongly undersaturated rocks (normative nepheline = 12–15 wt.%), with remarkable enrichment in Nb, Zr, Ti, and LREE (La_N/Sm_N ~ 30). The low Rb and K contents have been significantly altered during secondary analcite formation (Di Battistini et al., 1990).

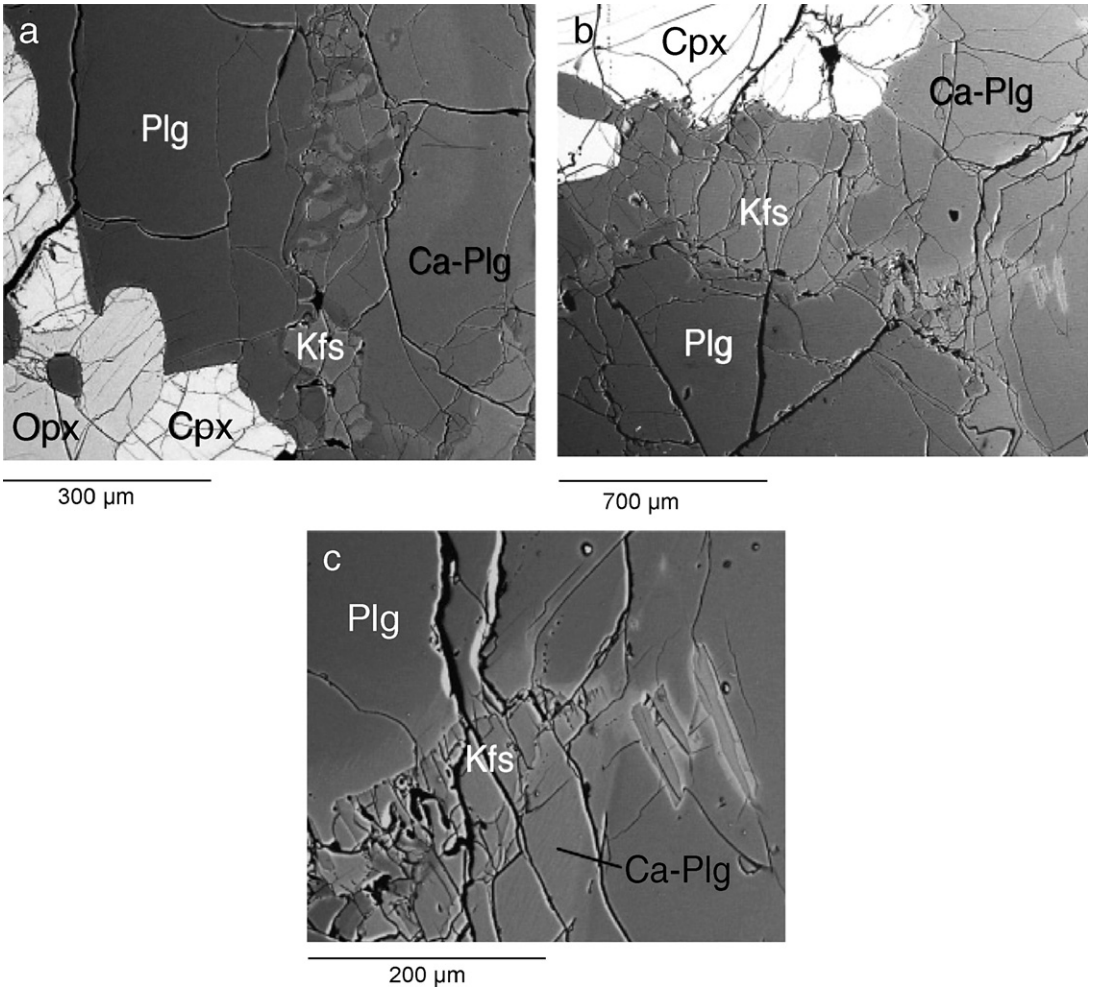

Fig. 6. BSE (back-scattered electron images) of myrmekite-like intergrowths of plagioclase with Ca-enriched plagioclase associated with K-feldspar along plagioclase–plagioclase grain boundaries.

Table 5
Whole-rock analyses of the metagabbronorite xenoliths (Gn) and host rock (Bn = basanite)

Sample	NB26 Gn	NB316 Gn	NB322 Gn	NB312 Gn	NB325 Gn	NB321 Gn	NB12 Gn	NB9 Gn	NB323 Gn	NB7 Gn	NB6 Gn	NB319 Gn	NB11 Gn	NB8 Gn	NB324 Gn	NB313 Gn	NB271 Gn	NB5 Gn	NB216 Bn
Major (wt.%) and trace element (ppm) abundances by X-ray fluorescence analyses																			
SiO_2	50.5	51.2	53.2	48.1	51.8	51.7	52.8	51.6	49.5	51.5	50.1	50.8	50.5	52.0	51.7	48.5	49.1	49.4	45.4
TiO_2	0.36	0.47	0.48	0.33	0.52	0.49	0.46	0.64	0.47	0.65	0.50	0.57	0.50	0.75	0.80	0.95	1.28	0.91	2.86
Al_2O_3	11.9	13.4	14.1	12.59	13.2	13.8	14.7	13.1	15.1	12.9	14.4	13.0	15.6	17.1	16.9	18.3	15.4	20.1	16.5
Fe_2O_3	8.92	9.07	8.29	10.35	9.37	9.52	8.49	9.49	9.66	9.60	8.87	10.75	9.57	8.21	8.97	10.45	12.16	8.65	10.54
MnO	0.17	0.18	0.17	0.18	0.18	0.18	0.18	0.20	0.17	0.21	0.22	0.20	0.21	0.16	0.18	0.14	0.29	0.14	0.18
MgO	13.29	12.18	10.70	13.25	11.22	10.99	9.53	10.31	10.47	10.35	9.44	10.54	8.30	7.07	6.25	7.13	7.94	4.98	5.49
CaO	11.43	10.41	9.22	11.76	10.75	10.05	9.83	11.51	11.93	11.34	12.61	11.27	11.69	10.57	10.19	11.03	9.44	11.99	8.97
Na_2O	0.92	0.98	1.99	0.89	1.16	1.60	2.01	1.62	0.96	1.83	1.29	1.35	1.67	2.04	2.61	1.59	2.69	2.24	5.11
K_2O	0.33	0.61	0.78	0.11	0.53	0.47	0.74	0.46	0.18	0.46	0.24	0.28	0.24	1.02	0.87	0.25	0.34	0.49	1.00
P_2O_5	0.04	0.09	0.11	0.04	0.09	0.04	0.09	0.06	0.03	0.04	0.07	0.06	0.04	0.21	0.20	0.04	0.01	0.06	0.70
LOI	1.12	0.43	0.07	1.52	0.09	0.09	0.28	0.00	0.44	0.00	1.30	0.00	0.59	0.00	0.30	0.41	0.36	0.10	2.63
	99.02																		
mg#	77.4	75.5	74.8	74.6	73.3	72.6	72.0	71.4	71.3	71.2	70.9	69.2	66.6	66.4	61.5	61.0	60.0	56.9	52.8
Ni	240	241	199	222	182	197	157	61	138	138	144	133	119	58	55	54	21	23	51
Co	55	57	43	53	52	48	45	30	46	47	44	45	45	29	35	37	35	30	29
Cr	912	939	680	967	714	671	569	206	509	517	494	536	508	203	181	175	8	56	52
Sc	44	41	35	48	45	–	38	49	50	47	38	50	46	35	37	36	–	26	19
V	209	175	167	156	186	213	171	186	290	298	194	244	218	184	210	585	177	357	200
Cu	17	13	8	20	18	16	12	41	45	39	30	28	20	42	18	66	100	26	–
Zn	80	71	75	233	82	85	78	79	176	80	89	93	69	73	82	72	111	55	–
Ga	5	12	14	12	13	14	15	14	10	13	16	14	18	20	21	22	16	24	–
Trace element abundances (ppm) by ICP-MS																			
Cs	<0.1	0.9	0.3	0.5	0.3	0.3	0.1	<0.1	0.4	<0.1	0.2	0.3	0.9	<0.1	0.5	0.4	<0.1	<0.1	–
Ba	86	135	166	68	172	134	189	110	61	118	261	93	92	240	308	101	118	148	2341
Rb	6	24	20	7	9	9	13	6	10	7	4	8	4	17	13	6	<1	14	86
Sr	157	194	209	210	190	216	233	209	220	211	271	205	283	226	258	307	286	321	1274
Zr	31	65	51	29	43	30	44	30	18	31	34	28	19	43	41	20	64	21	670
Nb	2.0	2.5	2.9	1.0	2.0	1.4	1.8	0.9	0.6	0.9	1.6	1.1	0.7	4.5	4.4	1.3	7.8	1.8	87.0
Y	11.0	15.6	17.1	14.6	20.3	14.0	18.3	18.7	11.1	19.5	18.9	18.5	13.3	18.6	19.8	9.9	22.2	10.1	35.0
La	3.40	8.79	9.11	6.22	8.21	4.79	9.33	5.06	4.58	5.21	7.81	5.01	4.90	14.27	12.42	10.00	7.62	6.00	78.0
Ce	7.90	18.90	19.00	7.37	19.10	10.50	19.80	12.20	–	12.50	20.20	12.10	9.26	28.60	26.00	15.60	16.20	11.90	146.0
Pr	1.11	2.36	2.26	1.77	2.51	1.40	2.45	1.75	1.28	1.82	2.75	1.69	1.38	3.34	3.21	1.63	2.12	1.43	–
Nd	5.69	10.60	10.30	7.38	12.10	6.89	11.20	9.14	6.20	9.44	13.00	8.48	6.83	14.60	14.40	7.12	10.40	6.62	59.0
Sm	1.69	2.58	2.59	2.02	3.19	1.97	2.91	2.75	1.72	2.93	3.36	2.57	1.94	3.38	3.45	1.72	2.96	1.69	8.60
Eu	0.52	0.60	0.79	0.696	0.79	0.71	0.89	0.86	0.59	0.91	1.00	0.87	0.74	0.96	1.04	0.66	1.02	0.81	2.59
Gd	1.85	2.24	2.27	2.33	3.09	2.11	2.65	3.06	1.95	3.19	2.96	2.77	2.08	2.54	2.81	1.73	3.21	1.54	7.22
Tb	0.32	0.42	0.46	0.4	0.58	0.39	0.51	0.57	0.32	0.57	0.52	0.50	0.37	0.49	0.52	0.28	0.63	0.30	1.02
Dy	2.12	2.74	3.00	2.42	3.77	2.45	3.23	3.44	2.08	3.61	3.34	3.29	2.40	3.34	3.61	1.90	3.94	2.01	4.72
Ho	0.43	0.55	0.59	0.49	0.74	0.50	0.64	0.68	0.40	0.71	0.66	0.65	0.48	0.66	0.70	0.36	0.84	0.40	–

Tm	0.18	0.24	0.27	0.206	0.34	0.23	0.29	0.30	0.17	0.31	0.26	0.30	0.20	0.28	0.30	0.15	0.39	0.16	–			
Yb	1.10	1.44	1.69	1.3	1.97	1.37	1.84	1.73	1.02	1.92	1.74	1.81	1.29	1.77	1.88	0.97	2.48	1.07	1.57			
Lu	0.16	0.21	0.24	0.203	0.29	0.20	0.26	0.26	0.15	0.27	0.25	0.26	0.19	0.25	0.27	0.14	0.37	0.15	0.20			
Trace element abundances (ppm) by ICP-MS																						
Hf	0.9	2.0	1.5	0.9	1.6	1.0	1.6	1.2	0.7	1.2	1.3	1.0	0.6	1.5	1.4	0.7	1.8	0.7	–			
Ta	0.04	0.10	0.12	0.03	0.12	0.01	0.05	<0.01	<0.01	<0.01	0.04	<0.01	<0.01	0.26	0.19	0.02	0.40	0.06	–			
Th	0.26	0.98	0.30	0.46	0.11	0.28	0.13	0.22	0.22	0.23	0.39	0.15	0.09	0.22	0.17	<0.05	0.17	0.16	14.20			
U	0.06	0.20	0.11	0.14	0.03	0.06	0.08	0.05	0.09	0.07	0.06	0.07	0.04	0.08	0.07	0.04	0.03	0.04	–			
Modal composition (vol.%)																						
pl	27.2	30.4	41.4	–	–	44.0	54.4	45.8	42.1	–	47.6	37.6	48.2	63.1	64.4	64.4	50.7	60.7	–			
cpx	39.0	25.0	22.4	–	–	15.7	17.7	30.0	23.3	–	30.2	29.0	25.0	16.9	15.4	19.5	35.7	22.2	–			
opx	31.7	32.8	30.1	–	–	36.5	18.5	19.0	27.6	–	18.0	30.6	19.0	18.3	11.5	11.6	5.7	11.9	–			
ox	2.1	6.1	3.0	–	–	0.8	6.8	5.1	6.8	–	1.2	2.6	7.6	1.4	8.3	3.1	7.9	4.5	–			
bt	–	5.4	0.8	–	–	3.0	–		0.2	–	–	0.2	–	0.3	–	1.2	–	–	–			
kfs	–	0.3	2.3	–	–	–	1.2	0.1	–	–	3.0	–	0.2	–	0.4	–	–	0.7	–			
rp	–	–	–	–	–	–	1.4	–	–	–	–	–	–	–	–	0.2	–	–	–			

(–) = not analyzed; mg# = 100 Mg/(Mg + 0.85$_{Fetot}$).
(–) = not analyzed; pl = plagioclase, cpx = clinopyroxene, opx = orthopyroxene, ox = oxides, bt = biotite, Kfs = K-feldspar; rp = reaction products.

5. Thermobarometric constraints

Equilibration temperatures have been calculated employing the two-pyroxene geothermometer of Wells (1977). Because of the large uncertainty in recalculating ferric iron, Fe^{2+} has been assumed to be Fe_{tot}. As a consequence, calculated temperatures represent maximum estimates. The obtained values for pairs of unexsolved clinopyroxene–orthopyroxene porphyroclasts and neoblasts are similar (respectively 902±28 to 914±39 °C). Application of the Brey and Kohler (1990) geothermometer gives temperatures about 50 °C lower than that of Wells (1977). However, the geothermometer of Brey and Kohler (1990) tends to underestimate the equilibration temperature if it is applied to minerals with higher Fe contents than those employed for the actual calibration of the geothermometer. The orthopyroxene-biotite geothermometer of Sengupta et al. (1990) tends to give lower values for the temperature, i.e. 850±10 °C.

The lack of garnet prevents accurate thermobarometry. However, an upper pressure limit of 1.0–1.2 GPa can be estimated by combining the calculated temperatures and the garnet-in curves for mafic compositions (Green and Ringwood, 1967; Wood, 1987). On the other hand, a lower pressure limit (~0.8 GPa) can be inferred from the occurrence of opx–cpx–spinel symplectites at the grain boundary interface between plagioclase and primary olivine (Johnson and Essene, 1982).

6. Source region of the metagabbronorite xenoliths

6.1. Deep-seated origin of the xenoliths and interactions with the host magmas

It has been pointed out (Rudnick, 1992) that caution must be used in the straightforward interpretation of metagabbronorite xenoliths as a direct sampling of the lower crust at the time of eruption. This is because granulite-facies rocks could have been transported to shallower levels by tectonic emplacement. However, a number of lines of evidence are consistent with a deep crustal provenance for the xenoliths: (i) the inferred P–T conditions of equilibration (T ~ 900 °C, P ~ 0.8–1.0 GPa) obviously record equilibration in the deep crust; (ii) no retrograde mineral changes (predictable in tectonically uplifted granulites) have been found; (iii) the highest grade terrains of the Palaeozoic basement (exposed in north-eastern Sardinia) do not exceed amphibolite-facies (Carmignani et al., 1994), and (iv) no upper crustal rocks (metamorphic rocks of lower grade, granites) have been sampled by the host lava.

The fine-grained coronas of olivine-clinopyroxene-K-feldspar surrounding the orthopyroxene likely result from reaction with an infiltrating alkali-rich silica-undersaturated melt. They are also observed at the xenolith-lava boundary and are very similar to the domains with pyrometamorphic textures described by Beccaluva et al. (2001) for the peridotite xenoliths from the same locality as the metagabbronorite xenoliths. However, extensive infiltration by a basanitic melt, in addition to in-situ crystallization and/or reaction with the xenolith constituents, is unlikely. The xenoliths showing corona reactions around orthopyroxene (i.e. samples NB9, NB26), do not display the anomalous abundances of trace elements (LREE, Nb, Zr) expected from significant contamination by the host magma.

6.2. Nature of the magmatic protoliths

Major and trace element composition of the xenoliths overall matches those of relatively undifferentiated subalkaline basaltic rocks (Table 5; Figs. 7–9). None of the xenoliths show the typical strong depletion in incompatible elements observed in cumulitic rocks because of small amounts of trapped liquid. The REE distribution gives further support to this view, because most patterns do not display features typically controlled by a cumulus of plagioclase or clinopyroxene, i.e. positive Eu anomaly or LREE-depletion with a convex upward shape. Finally, if we attempt to model the liquids in equilibrium with the xenoliths, assuming that they may represent cumulates, unrealistically high concentrations of incompatible elements and a marked Eu depletion are obtained, requiring evolved, silica-rich parent liquids (Fig. 10), which are not consistent with the observed high Mg#, Cr, and Ni of the bulk rock and generally high Mg# of both pyroxenes. However, those samples characterized by the highest Mg# and SiO_2/Al_2O_3 ratios coupled with high Cr (>600 ppm) may be affected by some accumulation of pyroxenes (Fig. 7; Table 5). Likewise, the low SiO_2/Al_2O_3 associated with the small positive Eu anomaly in samples NB313 and NB5 (Figs. 7 and 9, Table 5) likely reflect some enrichment in plagioclase, possibly due to metamorphic segregation. We can therefore reasonably conclude that most whole-rock compositions of the xenoliths correspond to frozen basaltic melts. The observed major and trace element variation trends may be consistent with a tholeiitic differentiation trend mainly controlled by removal of plagioclase+pyroxenes, whereas olivine crystallization (occurring only in one sample), was suppressed at an early stage.

The LILE-enriched and HFSE-depleted patterns of incompatible elements normalized to MORB, the low Ti/V (<20), as well as the Ti, Zr, and Y abundances (Pearce and Norry, 1979; Shervais, 1982) strongly argue for subduction-related basalts (low-K arc tholeiites) as parental magmas of the gabbronorite protoliths. The xenoliths display striking geochemical analogies (Fig. 9) with the rare primitive basaltic rocks erupted during the Miocene in Sardinia (Morra et al., 1997; Downes et al., 2001). In addition, they have Sr–Nd isotopic compositions ($^{87}Sr/^{86}Sr$=0.70578–0.70647, $^{143}Nd/^{144}Nd$=0.51240–0.51250; Montanini et al., 2002), which overlap the isotopically less enriched Tertiary basalts (Downes et al., 2001). Previous studies (e.g. Morra et al., 1997) have pointed out that the rarity of erupted primary basaltic magmas in the Tertiary calc-alkaline volcanism of Sardinia, compared to the high volumes of silicic ignimbrites and intermediate lavas, required ponding and differentiation of mafic liquids at lower to intermediate crustal levels. The metagabbronorite xenoliths are therefore potential key-rock types for testing petrogenetic models for the origin of the voluminous Miocene ignimbrites of Western Sardinia as well as characterization of the new crust added by Tertiary subduction-related magmatism. Alternatively, the xenoliths could be older, subduction-related rocks (possibly related to the Variscan orogeny), which underwent subsolidus recrystallization in the lower crust and likely reheating due to the protracted magmatic activity of Sardinia during Tertiary times. In both cases, the occurrence of the olivine-plagioclase reaction leading to pyroxene-spinel symplectitic intergrowths suggests that at least one stage of near-isobaric cooling has occurred during the subsolidus history of these rocks (Griffin and Heier, 1973; Johnson and Carlson, 1990).

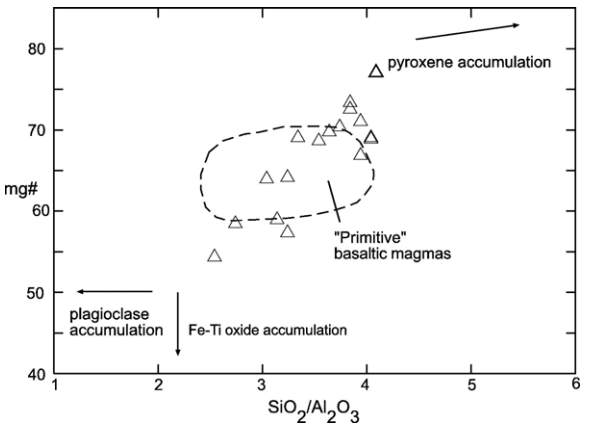

Fig. 7. Plot of whole-rock Mg# and SiO_2/Al_2O_3 values for the metagabbronorite xenoliths. Fields of primitive basaltic magmas and compositional vectors produced by accumulation of pyroxene, plagioclase and Fe–Ti oxides after Kempton and Harmon (1992).

6.3. Implications for the lower crust composition beneath Sardinia and comparison with the geophysical data

At pressure of 0.8–1.0 GPa, mean temperatures of 850–900 °C indicate subsolidus equilibration under granulite-facies conditions. The temperatures estimated for the metagabbronorite xenoliths are consistent with those inferred for peridotite xenoliths from the uppermost mantle of Sardinia (~1000 °C, Zerbi et al., 1978; Rutter, 1987; 870–1000 °C, Beccaluva et al., 2001). In general, temperatures in excess of 900 °C are common among lower crustal xenoliths originating in rift zones or areas of recent magmatic activity. Such temperatures are generally higher than those calculated for most xenoliths originating from Hercynian Europe (Downes, 1993). One exception are the temperatures estimated for the xenoliths from two areas characterized by high heat-flow (Pannonian basin: Kempton et al., 1997; Embey-Isztin et al., 2003 and Northern Hessian Depression: Mengel, 1990), i.e. two crustal sections affected by the Alpine orogenesis and by continental rifting, respectively.

Geophysical studies of the Sardo–Corsican microplate (Egger et al., 1988; Peruzza et al., 1990) have shown a normal continental structure beneath Sardinia,

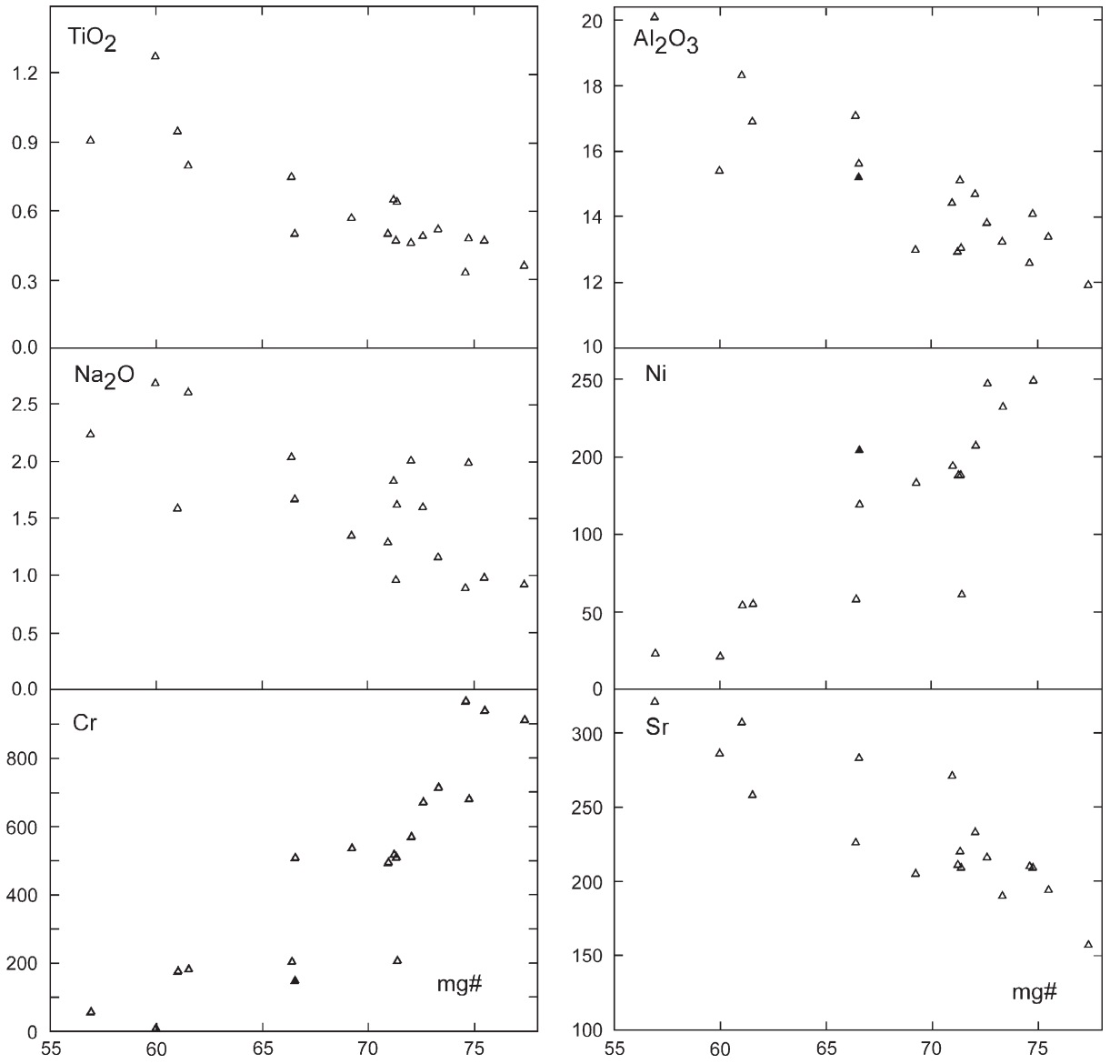

Fig. 8. Plot of whole-rock Mg# vs. TiO_2, Al_2O_3, Na_2O (wt.%), Ni, Cr and Sr (ppm) for the metagabbronorite xenoliths.

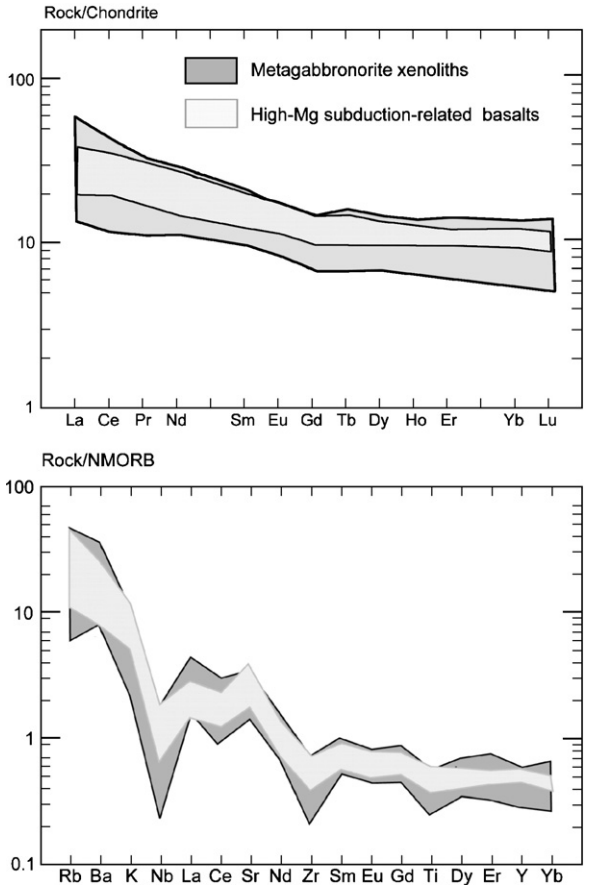

Fig. 9. (a) Chondrite-normalized whole-rock REE abundances of the metagabbronorite xenoliths (normalizing values after Anders and Grevess, 1989); (b) MORB-normalized incompatible trace element abundances diagram for the metagabbronorite xenoliths (normalizing values after Sun and McDonough, 1989). Data for Tertiary subduction-related basaltic rocks from Sardinia after Downes et al. (2001) and Morra et al. (1997).

relatively unmodified by Miocene drifting away from the European continental margin, with a crustal thickness of 30–32 km beneath the central-western sector. An estimate of the seismic P-wave velocity in the xenoliths has been carried out and the resulting values have been compared with those measured for the deep crust in order to test the likelihood that these rocks are samples of the lower crust. V_p can be obtained by combining the modal composition of the rocks with the experimental V_p values of each mineral taken from the literature (Christensen, 1989) and assuming that the porosity at high pressure is negligible. To this purpose, a simplified four-phase assemblage with the average modal composition of the investigated xenoliths (plagioclase: 48.1%, clinopyroxene: 25.5 vol.%, orthopyroxene: 21.6%, magnetite: 4.5 vol.%) has been adopted. The employed temperatures and pressure derivatives for the seismic velocity are given in Furlong and Fountain (1986). Corrections have been made for $P=1$ GPa and $T=600$ °C which represents the present-day temperature, calculated from heat flow data, for the lowermost crust beneath Sardinia (Dalla Vedova et al., 1995). The resulting V_p (7.12 km s^{-1}) are in good agreement with the values reported for central-western Sardinia by seismic refraction surveys, i.e. V_p progressively changes from 6.75 to 7.3 km s^{-1} at depths of between 25 and 30 km (Peruzza et al., 1990). The gabbronorite xenoliths may be thus considered as plausible constituents of the Sardinia lower crust.

7. Origin of K-feldspar and high-grade KCl-rich fluid metasomatism

The possible origin of these K-feldspar textures in the xenoliths through magmatic crystallization or as a result of closed-system metamorphic reaction (e.g. biotite breakdown) cannot be a priori excluded. However, textural and geochemical evidences argue against these hypotheses and point to a role for metasomatic alteration. The preservation of K-feldspar as micro-veins and as myrmekite-like textures at plagioclase–plagioclase grain boundary interfaces in extensively re-crystallized and foliated metaigneous rocks cannot be obviously explained by magmatic crystallization. For example, there is no evidence for a significant correlation between SiO_2 and K_2O as would be expected

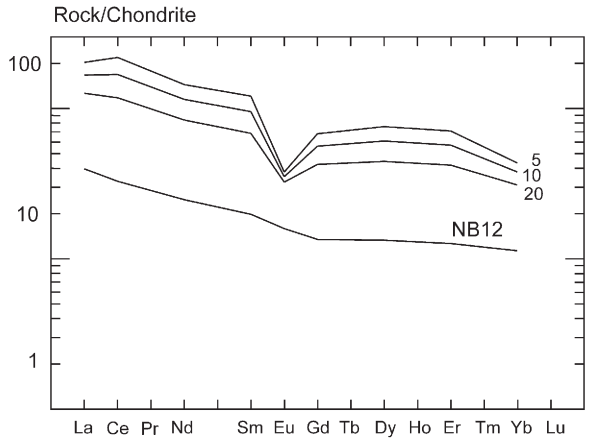

Fig. 10. REE modelisation of the parental liquid compositions from the sample NB12 considered as a plagioclase+orthopyroxene+clinopyroxene cumulate rock (phase proportions in the solid: plagioclase=60%, clinopyroxene=20%, orthopyroxene=20%) with variable amounts of trapped residual melt. Calculations were carried out according to the procedure of Bedard (1994) that is based on whole-rock trace element concentrations. Numbers on the patterns refer to trapped melt percentages used for the calculations. Partition coefficient for plagioclase, ortho- and clinopyroxenes taken from Bindeman et al. (1998), Dunn and Sen (1994) and Hart and Dunn (1993).

from an ordinary magmatic fractionation trend. Also, K-feldspar formation due to either biotite dehydration or dehydration melting is not tenable for the following reasons: (i) Ti-rich biotite occurring in several xenoliths gives all indication of being stable (only locally, might heating of this biotite in the host magma yield fine-grained breakdown products including K-feldspar + ilmenite + orthopyroxene, see Section 4.1); (ii) K-feldspar is commonly associated with plagioclase and it does not show inclusions or intergrowths with other phases possibly derived from biotite + plagioclase reaction (e.g. garnet, orthopyroxene, Fe–Ti oxides, see Patiño Douce and Beard, 1995). In contrast, the occurrence of K-feldspar as micro-veins, myrmekitic intergrowths with plagioclase, and randomly distributed antiperthites ("replacement antiperthites", c.f. Griffin, 1969) is consistent with a metasomatic origin and requires an external K-rich fluid source.

A number of workers have documented and subsequently speculated as to the role of KCl brines or K-rich fluids in the lower crust and upper mantle. This documentation includes high grade rocks exposed by erosion (Hansen et al., 1995; Newton et al., 1998; Harlov et al., 1998; Harlov and Förster, 2002; Fiannacca et al., 2005), xenoliths from the lower crust and upper mantle (e.g. Perchuk et al., 2002; Harlow and Davies, 2004; Kressig and Elliott, 2005), kimberlites (Kamenetsky et al., 2004), as well as brine-rich inclusions in diamonds (Izraeli et al., 2001; Klein-benDavid et al., 2004; Izraeli et al., 2004; see also Tomlinson et al., 2004). While the presence of apatite (nominally fluorapatite) has been generally noted in samples of rock from both the lower crust and upper mantle, which are known to have undergone some form of metasomatism (e.g., King et al., 2003; Seyler et al., 2004), less attention has been paid to its composition though, when analysed by EMP, such 'fluorapatites' tend to show very high levels of both Cl and OH and, when analysed using IR, possible high levels of CO_2 as well (e.g. O'Reilly and Griffin, 2000; Carswell and van Roermund, 2005). This suggests that they either formed in the presence of Na–K–Ca-brines/CO_2-rich fluids or else were metasomatised by such fluids.

In the metagabbronorite xenoliths of the present study, the textural occurrence of K-feldspar and its associated geochemical features, coupled with the high Cl and OH content of the fluorapatites, could be explained as being due to metasomatism by a K-rich brine with probable minor Na and Ca components. This metasomatism could have occurred both during as well as after granulite-facies recrystallization of the xenoliths. In such a scenario, the passage of K-rich brines, through that area of the lower crust from which these xenoliths originate, first resulted in the formation of K-feldspar–plagioclase intergrowths along plagioclase–plagioclase and plagioclase–pyroxene grain boundaries (Fig. 6). Continued passage of the K-rich brines was subsequently followed by the formation of true K-feldspar micro-veins. At some later stage, local, partial recrystallization of these micro-veins occurred resulting in thicker more massive mineral grains, though still forming apparent veins throughout the rock (Fig. 5). During the formation of the K-feldspar micro-veins, diffusion of K into random plagioclase grains led to the nucleation of K-feldspar blebs and rods within the interior of the plagioclase grain resulting in replacement antiperthite along with its characteristic enrichment in Ca along the rim of the lamellae (Figs. 3 and 4). The randomness of this texture suggests that it was mainly controlled by the composition of a metasomatising fluid, e.g. Albite + K + (fluid) = Orthoclase + Na + (fluid). Discrete, more isolated, anhedral grains of K-feldspar could have resulted from the further enlargement and then recrystallization of the K-feldspar micro-veins into discrete crystals surrounded by plagioclase showing 120° triple junctions with the adjacent minerals (Fig. 2f). The presence of albite exsolution lamellae in the K-feldspar could be indicative of a Na component in the infiltrating brine coupled with some cation exchange with the surrounding plagioclase (cf. Table 4). It is also probable that the formation of these K-feldspar micro-veins and replacement anti-perthite could have been the result of several stages or pulses of K-rich fluid infiltration.

The presence of a K-, Na-, and Ca-bearing metasomatic brine is also strongly supported by the high Cl and OH content in the fluorapatite (Table 3). It should be cautioned that a portion or perhaps all of the calculated OH component in the fluorapatite could be CO_2 (cf. O'Reilly and Griffin, 2000) since neither OH nor CO_2 was directly measured. Experimentally, it has been demonstrated that fluorapatite gains copious amounts of Cl in the presence of even minor concentrations of $CaCl_2$ brines under conditions quite similar to those under which these xenoliths were metasomatised (cf. Harlov and Förster, 2003).

As to the origin of these metasomatising fluids, they could be highly saline residual brines given off during the solidification of mafic bodies underplating the lower crust (and providing the heat necessary for granulite-facies metamorphism), as originally proposed by Harlov and Förster (2002) for the Ivrea–Verbano Zone granulites (see also Franz and Harlov, 1998). However, a deep-seated provenance from the underlying lithospheric mantle may be also envisaged. Though, in retrospect, it is unlikely that metasomatic processes associated with recent alkaline magmatic activity on Sardinia could be responsible for these K-feldspar features. This is because, the partial to

extensive textural equilibration of these metasomatically induced K-feldspar features would argue against the probable short time span between the actual metasomatic event and subsequent eruption. An exception to this could be the fine-grained coronas with olivine + clinopyroxene + Ba-rich K-feldspar that were probably formed by reaction with an alkaline silicate melt related to the Pliocene activity. These coronas are comparable to the pyrometamorphic textured domains within the mantle xenoliths that are considered to be later than the cryptic LREE and isotope enrichment in the clinopyroxene. Whether mantle xenoliths from this region also show the same type of metasomatism is uncertain. For example, in studies of shallow mantle xenoliths from Sardinia (Beccaluva et al., 2001), fluorapatite of metasomatic origin has never been reported. The metasomatic imprint, as evidenced by LREE enrichment and Sr–Nd isotopes in clinopyroxene, has been attributed to alkaline mafic melts with EM-like characteristics migrating through the lithosphere. However, this is not a definite argument against metasomatising brines originating in the lithospheric mantle since sampling of the mantle by xenoliths is at best random.

In conclusion, the various lines of evidence presented in this study support the premise that formation of K-feldspar in these mafic xenoliths and enrichment of fluorapatite in Cl is a reflection of metasomatic processes, which required an external K-rich fluid source. This fluid source probably took the form of a K-bearing brine with minor Na and Ca components, which operated in the lower crust beneath Sardinia during and after in-situ re-equilibration of mafic igneous rocks under granulite-facies conditions.

Acknowledgements

Dieter Rhede and Oona Appelt (GFZ, Potsdam) are thanked for the support with the electron microprobe. Helga Kemnitz is acknowledged for the assistance with the SEM. Filippo Ridolfi is thanked for reducing the fluorapatite EMP data. We are grateful for the reviews and comments by S. Arai, W.L. Griffin and E. Hansen. This work was supported by the Italian MIUR funds.

References

Anders, E., Grevess, N., 1989. Abundances of the elements; meteoritic and solar. Geochimica et Cosmochimica Acta 53, 197–214.

Aoki, K., Kushiro, I., 1968. Some clinopyroxenes from ultramafic inclusions in Dreiser Weiher, Eifel. Contributions to Mineralogy and Petrology 18, 326–337.

Assorgia, A., Balogh, K., Lecca, L., Ibba, A., Porcu, A., Secchi, F., Tilocca, G., 1995. Volcanological characters and structural context of Oligo-Miocene volcanic successions from Central Sardinia (Italy). In: Polino, R., Sacchi, R. (Eds.), Rapporti tra Alpi e Appennino. Accademia Nazionale delle Scienze, vol. 14, pp. 397–424.

Beccaluva, L., Deriu, M., Macciotta, G., Savelli, C., Venturelli, G., 1977. Geochronology and magmatic character of the Pliocene–Pleistocene volcanism in Sardinia (Italy). Bullettin of Volcanology 40, 153–168.

Beccaluva, L., Civetta, L., Macciotta, G., Ricci, C.A., 1985. Geochronology in Sardinia: results and problems. Rendiconti della Società Italiana di Mineralogia e Petrologia 40, 153–168.

Beccaluva, L., Macciotta, G., Siena, F., Zeda, O., 1989. Harzburgite–lherzolite xenoliths and clinopyroxene megacrysts of alkaline basic lavas from Sardinia. Chemical Geolology 77, 331–345.

Beccaluva, L., Bianchini, G., Coltorti, M., Perkins, W.T., Siena, F., Vaccaro, C., Wilson, M., 2001. Multistage evolution of the European lithospheric mantle: new evidence from Sardinian peridotite xenoliths. Contributions to Mineralogy and Petrology 142, 284–297.

Bedard, J.H., 1994. A procedure for calculating the equilibrium distribution of trace elements among the minerals of cumulate rocks, and the concentration of trace elements in the coexisting liquids. Chemical Geology 118, 143–153.

Bindeman, I.N., Davis, A.M., Drake, M.J., 1998. Ion microprobe study of plagioclase-basalt partition experiments at natural concentration levels of trace elements. Geochimica et Cosmochimica Acta 62, 1175–1193.

Brey, G.P., Kohler, T., 1990. Geothermometry in four-phase Lherzolites II. New thermobarometers, and practical assesment of existing thermobarometers. Journal of Petrology 31, 1353–1378.

Carmignani, L., Carosi, R., Di Pisa, A., Gattiglio, M., Musumeci, G., Oggiano, G., Pertusati, P.C., 1994. The Hercynian chain in Sardinia (Italy). Geodinamica Acta 7, 31–47.

Carswell, D.A., van Roermund, H.L.M., 2005. On multi-phase mineral inclusions associated with microdiamond formation in mantle-derived peridotite lens at Bardane on Fjortoft, west Norway. European Journal of Mineralogy 17, 31–42.

Christensen, N.I., 1989. Constitution of the lower continental crust based on experimental studies of seismic velocities in granulite. Geological Society America Bulletin 86, 227–236.

Coulon, C., 1977. Le vulcanisme calco-alcalin cénozoique de Sardaigne (Italie). Petrographie, géochimie et genése des laves andésitiques et des ignimbrites-signification géodinamique. Thése Doct., Univ. Aix-Marseille III, pp. 288.

Dalla Vedova, B., Lucazeau, F., Pasquale, F., Pellis, M., Verdoya, G., 1995. Heat flow in the tectonic provinces crossed by the southern segment of the European Geotraverse. Tectonophysics 244, 57–74.

de Albuquerque, C.A.R., Capedri, S., Dostal, J., 1977. Mineralogy of spinel peridotite inclusions of alkali basalts from Sardinia. Geological Society of America Bulletin 88, 1493–1496.

Di Battistini, G., Montanini, A., Zerbi, M., 1990. Geochemistry of volcanic rocks from southern Montiferro (Western Sardinia, Italy). Neues Jahrbuch für Mineralogie Abhandlungen 162, 35–67.

Dostal, J., Capedri, S., 1976. Uranium in spinel peridotite inclusions in basalts from Sardinia. Contributions to Mineralogy and Petrology 54, 245–254.

Dostal, J., Coulon, C., Dupuy, C., 1982. Cenozoic andesitic rocks of Sardinia (Italy). In: Thorpe, R.S. (Ed.), Andesites. Wiley, New York, pp. 353–370.

Downes, H., 1993. The nature of the lower continental crust of Europe: petrological and geochemical evidence from the xenoliths. Physics of Earth and Planetary Interiors 79, 195–218.

Downes, H., Thirlwall, M.F., Trayhorn, S.C., 2001. Miocene subduction-related magmatism in southern Sardinia: Sr–Nd- and oxygen

isotopic evidence for mantle source enrichment. Journal of Volcanology and Geothermal Research 106, 1–21.

Dunn, T., Sen, C., 1994. Mineral/matrix partition coefficients for orthopyroxene, plagioclase, and olivine in basaltic to andesitic systems. Geochimica et Cosmochimica Acta 58, 717–733.

Egger, A., Demartin, M., Ansorge, G., Banda, E., Maistrello, M., 1988. The gross structure of the crust under Corsica and Sardinia. Tectonophysics 150, 363–389.

Embey-Isztin, A., Downes, H., Kempton, P.D., Dobosi, G., Thirlwall, M., 2003. Lower crustal granulite xenoliths from the Pannonian Basin, Hungary. Part 1: mineral chemistry, thermobarometry and petrology. Contributions to Mineralogy and Petrology 144, 652–670.

Fiannacca, P., Brotzu, P., Cirrincione, R., Mazzoleni, P., Pezzino, A., 2005. Alkali metasomatism as a process for trondhjemite genesis: evidence from Aspromonte Unit, north-eastern Peloritani, Sicily. Mineralogy and Petrology 84, 19–45.

Franz, L., Harlov, D.E., 1998. High-grade K-feldspar veining in granulites from the Ivrea–Verbano Zone, northern Italy: fluid flow in the lower crust and implications for granulites facies genesis. Journal of Geology 106, 455–472.

Furlong, K.P., Fountain, D.M., 1986. Continental crustal underplating: thermal considerations and seismic–petrologic consequences. Journal of Geophysical Research 91, 8285–8294.

Gallo, F., Giammetti, F., Vernia, L., 1974. Studio geo-petrografico delle vulcaniti post-mioceniche del Montiferro nord-orientale. Ateneo Parmense. Acta Naturalia 10, 121–182.

Green, D.H., Ringwood, A.E., 1967. An experimental investigation of the gabbro to eclogite transformation and its petrological applications. Geochimica et Cosmochimica Acta 31, 767–833.

Griffin, W.L., 1969. Replacement antiperthite in gneisses of the Babbit-Embarrass area, Minnesota, USA. Lithos 2, 171–186.

Griffin, W.L., Heier, K.S., 1973. Petrological implications of some corona structures. Lithos 6, 315–335.

Griffin, W.L., O'Reilly, S.Y., 1987. The composition of the lower crust and the nature of the continental Moho-xenolith evidence. In: Nixon, P.H. (Ed.), Mantle Xenoliths. Elsevier, Amsterdam, pp. 413–430.

Hansen, E.C., Newton, R.C., Janardhan, A.S., Lindenberg, S., 1995. Differentiation of late Archean crust in the eastern Dharwar Craton, Krishnagiri-Salem Area, South India. Journal of Geology 103, 629–651.

Harlov, D.E., Förster, H.-J., 2002. High-grade fluid metasomatism on both a local and regional scale: the Seward Peninsula, Alaska and the Val Strona di Omegna, Ivrea-Verbano Zone, northern Italy part I: petrography and silicate mineral chemistry. Journal of Petrology 43, 769–799.

Harlov, D.E., Förster, H.J., 2003. Fluid-induced nucleation of (Y+REE)-phosphate minerals within apatite: nature and experiment. Part II. Fluorapatite. American Mineralogist 88, 1209–1229.

Harlov, D.E., Hansen, E.C., Bigler, C., 1998. Petrologic evidence for K-feldspar metasomatism in granulite facies rocks. Chemical Geology 151, 373–386.

Harlov, D.E., Förster, H.-J., Nijland, T.G., 2002. Fluid-induced nucleation of REE-phosphate minerals in apatite: nature and experiment. Part I. Chlorapatite. American Mineralogist 87, 245–261.

Harlow, G.E., Davies, R., 2004. Status report on stability of K-rich phases at mantle conditions. Lithos 77, 647–653.

Hart, S.R., Dunn, T., 1993. Experimental Cpx/melt partitioning of 24 trace elements. Contributions to Mineralogy and Petrology 113, 1–8.

Izraeli, E.S., Harris, J.W., Navon, O., 2001. Brine inclusions in diamonds; a new upper mantle fluid. Earth and Planetary Science Letters 187, 323–332.

Izraeli, E.S., Harris, J.W., Navon, O., 2004. Fluid and mineral inclusions in cloudy diamonds from Koffiefontein, South Africa. Geochimica et Cosmochimica Acta 68, 2561–2575.

Jarosewich, E., Boatner, L.A., 1991. Rare-earth element reference samples for electron microprobe analysis. Geostandards Newsletter 15, 397–399.

Jarosewich, E., Nelen, J.A., Norberg, J.A., 1980. Reference samples for electron microprobe analysis. Geostandards Newsletter 4, 43–47.

Johnson, C.A., Essene, E.J., 1982. The formation of garnet in olivine-bearing metagabbros from the Adirondacks. Contributions to Mineralogy and Petrology 81, 240–251.

Johnson, J.D., Carlson, W.D., 1990. The origin of olivine-plagioclase reaction in metagabbros from the Adirondack mountains, New York. Journal of Metamorphic Geology 8, 697–717.

Kamenetsky, M.B., Sobolev, A.V., Kamenetsky, V.S., Maas, R., Danyushevsky, L.V., Thomas, R., Pokhilenko, N.P., Sobolev, N.V., 2004. Kimberlite melts rich in alkali chlorides and carbonates; a potent metasomatic agent in the mantle. Geology 32, 845–848.

Kay, R.W., Kay, S.M., 1984. Petrology and geochemistry of the lower continental crust: an overview. In: Dawson, J.B., Carswell, D.A., Hall, J., Wedepohl, K.H. (Eds.), The Nature of the Lower Continental Crust. Geological Society Special Publication 24, pp. 147–159.

Kempton, P.D., Harmon, R.S., 1992. Oxygen isotope evidence of large-scale hybridization of the lower crust during magmatic underplating. Geochimica et Cosmochimica Acta 54, 3401–3426.

Kempton, P.D., Downes, H., Embey-Isztin, A., 1997. Mafic granulite xenoliths in Neogene alkali basalts from the Western Pannonian Basin: insights into the lower crust of a collapsed orogen. Journal of Petrology 38, 941–970.

King, R.L., Kohn, M.J., Eiler, J.M., 2003. Constraints on the petrologic structure of the subduction zone slab-mantle interface from Franciscan Complex exotic ultramafic blocks. Geological Society of America Bulletin 115, 1097–1109.

Klein-ben David, O., Izraeli, E.S., Hauri, E., Navon, O., 2004. Mantle fluid evolution — a tale of one diamond. Lithos 77, 243–253.

Kressig, K., Elliott, T., 2005. Ca isotope fingerprints of early crust–mantle evolution. Geochimica et Cosmochimica Acta 69, 165–176.

Kushiro, I., 1969. The system forsterite-diopside-silica with and without water at high pressures. American Journal of Science 267A, 269–294.

Leake, B.E., Woolley, A.R., Arps, C.E.S., et al., 1997. Nomenclature of amphiboles: report of the subcommittee on amphiboles of the International Mineralogical Association, commission on new minerals and mineral names. American Mineralogist 82, 1019–1037.

Lecca, L., Lonis, R., Luxoro, S., Melis, E., Secchi, F., Brotzu, P., 1997. Oligo-Miocene volcanic sequences and rifting stages in Sardinia; a review. In: Brotzu, P. (Ed.), The Tertiary Calcalkaline Volcanism of Sardinia. Periodico di Mienralogia, vol. 66, pp. 7–61.

Lustrino, M., Melluso, L., Morra, V., 2002. The transition from alkaline to tholeiitic magmas: a case study from the Orosei-Dorgali Pliocene volcanic district (NE Sardinia, Italy). Lithos 63, 83–113.

Mengel, K., 1990. Crustal xenoliths from Tertiary volcanics of the Northern Hessian Depression. Contributions to Mineralogy and Petrology 104, 8–26.

Mezger, K., 1992. Temporal evolution of regional granulite terranes: implications for the formation of the lower continental crust. In: Kay, R.W., Arculus, S.J., Fountain, D.M. (Eds.), Lower Continental Crust. Elsevier, Amsterdam, pp. 447–472.

Monaghan, A., 2001. Coeval extension, sedimentation and volcanism along the Cainozoic rift system of Sardinia. In: Ziegler, P.A., Cavazza, W., Robertson, A.H.F. (Eds.), Peri-Tethys Memoir 6; Peri-Tethyan Rift/Wrench Basins and Passive Margins Memoires du Museum National d'Histoire Naturelle, vol. 186, pp. 707–734.

Montanini, A., Zerbi, M., Toscani, L., 1992. Petrology of deep-seated spinel-rich gabbroic and pyroxenite xenoliths from Montiferro volcanic complex. Mineralogica et Petrographica Acta 25, 77–98.

Montanini, A., Meli, S., Thoni, M., Castorina, F., 2002. Granulite-facies mafic xenoliths in the Pliocene alkaline volcanics from western Sardinia (Italy): evidence for recent subduction-related lower crustal accretion in the Sardinia–Corsica microplate ? 18th General Meeting of the International Mineralogical Association, Edimburgh (UK), Abstract Volume, p. 223.

Montigny, R., Edel, J.B., Thuizat, R., 1981. Oligo-Miocene rotation of Sardinia: K–Ar ages and paleomagnetic data of Tertiary volcanics. Earth and Planetary Science Letters 54, 261–271.

Morra, V., Secchi, F., Melluso, L., Franciosi, L., 1997. High-Mg subduction-related Tertiary basalts in Sardinia, Italy. Lithos 40, 69–91.

Newton, R.C., Aranovich, L. Ya., Hansen, E.C., Vandenheuvel, B.A., 1998. Hypersaline fluids in Precambrian deep-crustal metamorphism. Precambrian Research 91, 41–63.

O'Reilly, S.Y., Griffin, W.L., 2000. Apatite in the mantle: implications for metasomatic processes and high heat production in Phanerozoic mantle. Lithos 53, 217–232.

Patiño Douce, A.E., 1993. Titanium substitution in biotite: an empirical model with applications to thermometry, O_2 and H_2O barometries, and consequences for biotite stability. Chemical Geology 108, 133–162.

Patiño Douce, A.E., Beard, J.S., 1995. Dehydration-melting of biotite gneiss and quartz amphibolite from 3 to 15 kbar. Journal of Petrology 36, 707–738.

Pearce, J.A., Norry, M.J., 1979. Petrogenetic implications of Ti, Zr, Y and Nb variations in volcanic rocks. Contributions to Mineralogy and Petrology 69, 33–47.

Perchuk, L.L., Safonov, O.G., Yapaskurt, V.O., Barton Jr., J.M., 2002. Crystal equilibria involving potassium-bearing clinopyroxene as indicator of mantle-derived ultrahigh-potassic liquids: an analytical review. Lithos 60, 89–111.

Percival, J.A., Fountain, D.M., Salibury, M.H., 1992. Exposed crustal cross-sections as windows of the lower crust. In: Fountain, D.M., Arculus, R., Kay, R.W. (Eds.), Continental Lower Crust. Elsevier, Amsterdam, pp. 317–319.

Peruzza, L., Fischer, G., Schnegg, P.A., Ranieri, G., 1990. Analysis of the Sardinian NS magnetotelluric profile. In: Freeman, R., Giese, P., Mueller, S. (Eds.), European Geotraverse; Integrative Studies; Results from the Fifth Earth Science Study Centre. European Science Foundation, Strasbourg, pp. 329–346.

Pouchou, J.L., Pichoir, F., 1985. "PAP" (φ–ρ–Z) procedure for improved quantitative microanalysis. In: Armstrong, J.T. (Ed.), Microbeam Analysis. San Francisco Press, San Francisco, pp. 104–106.

Rock, N.M.S., 1990. The International Mineralogical Association (IMA/CNMMN) pyroxene nomenclature scheme: computerization and its consequences. Mineralogy and Petrology 43, 99–119.

Rudnick, R.L., 1992. Xenoliths-samples of the lower continental crust. In: Fountain, D.M., Arculus, R., Kay, R.W. (Eds.), Continental Lower Crust. Elsevier, Amsterdam, pp. 269–316.

Rudnick, R.L., Taylor, S.L., 1987. The composition and petrogenesis of the lower crust: a xenolith study. Journal of Geophysical Research 92, 13981–14005.

Rutter, M.J., 1987. The nature of the litosphere beneath the Sardinian continental block: mantle and deep crustal inclusions in mafic alkaline lavas. Lithos 20, 225–234.

Savelli, C., Beccaluva, L., Deriu, M., Macciotta, G., Maccioni, L., 1979. K–Ar geochronology and evolution of the Tertiary calc-alkalic volcanism of Sardinia (Italy). Journal of Volcanology and Geothermal Research 5, 257–269.

Selverstone, J., Stern, C.R., 1983. Petrochemistry and recrystallization history of granulite xenoliths from the Pali-Aike volcanic field, Chile. American Mineralogist 68, 1102–1112.

Sengupta, S., Dasgupta, P.K., Bhattacharya-Mukherjee, M., 1990. An orthopyroxene-biotite geothermometer and its application in crustal granulites and mantle-derived rocks. Journal of Metamorphic Geology 8, 191–197.

Seyler, M., Lorand, J.-P., Toplis, M.J., Godard, G., 2004. Asthenospheric metasomatism beneath the mid-ocean ridge: evidence from depleted abyssal peridotites. Geology 32, 301–304.

Shervais, J.W., 1982. Ti-V plots and the petrogenesis of modern and ophiolitic lavas. Earth and Planetary Science Letters 59, 101–118.

Speranza, F., Villa, I.M., Sagnotti, L., Florindo, F., Cosentino, D., Cipollari, P., Mattei, M., 2002. Age of the Corsica-Sardinia rotation and Liguro-Provencal Basin spreading: new paleomagnetic and Ar/Ar evidence. Tectonophysics 347, 231–251.

Stormer Jr., J.C., Pierson, M.J., Tacker, R.C., 1993. Variation of F and Cl X-ray intensity due to anisotropic diffusion of apatite during electron microprobe analyses. American Mineralogist 78, 641–648.

Sun, S.S., McDonough, F., 1989. Chemical and isotopic systematics of oceanica basalts: implications for mantle composition and processes. In: Saunders, A.D., Norry, M.J. (Eds.), Magmatism in the Oceanic Basins, Geol. Soc. London Spec. Publ., vol. 42, pp. 313–345.

Tomlinson, E., Jones, A., Milledge, J., 2004. High-pressure experimental growth of diamond using C–K_2CO_3–KCl as an analogue for Cl-bearing carbonate fluid. Lithos 77, 287–294.

Weber, M.B.I., Tarney, J., Kempton, P.D., Kent, R.W., 2002. Crustal make-up of the Northern Andes: evidence based on deep crustal xenolith suites, Mercaderes, SW Colombia. Tectonophysics 345, 49–82.

Wells, P.R.A., 1977. Pyroxene thermometry in simple and complex systems. Contributions to Mineralogy and Petrology 62, 129–139.

Wood, B.J., 1987. Thermodynamics of multicomponent systems containing several solid solutions. In: Carmichael, I.S.E., Eugster, H.P. (Eds.), Thermodynamic Modelling of Geologic Materials: Minerals, Fluids and Melts. Mineralogical Society of America, Washington D.C., pp. 71–95.

Zerbi, M., Giammetti, F., Gallo, F., Vernia, L., 1978. Petrografia degli inclusi femici e ultrafemici delle basaniti analcitiche del Montiferro, Sardegna. Ateneo Parmense. Acta Naturalia 14, 311–337.